



**HAL**  
open science

## Measurements and computational analysis on the natural decay of $^{176}\text{Lu}$

F.G.A. Quarati, G. Bollen, P. Dorenbos, M. Eibach, K. Gulyuz, A. Hamaker, C. Izzo, D.K. Keblbeck, Xavier Mougeot, D. Puentes, et al.

► **To cite this version:**

F.G.A. Quarati, G. Bollen, P. Dorenbos, M. Eibach, K. Gulyuz, et al.. Measurements and computational analysis on the natural decay of  $^{176}\text{Lu}$ . *Physical Review C - Nuclear Physics*, 2023, 107, pp.024313. 10.1103/PhysRevC.107.024313 . cea-04021301

**HAL Id: cea-04021301**

**<https://cea.hal.science/cea-04021301>**

Submitted on 9 Mar 2023

**HAL** is a multi-disciplinary open access archive for the deposit and dissemination of scientific research documents, whether they are published or not. The documents may come from teaching and research institutions in France or abroad, or from public or private research centers.

L'archive ouverte pluridisciplinaire **HAL**, est destinée au dépôt et à la diffusion de documents scientifiques de niveau recherche, publiés ou non, émanant des établissements d'enseignement et de recherche français ou étrangers, des laboratoires publics ou privés.

# Measurements and computational analysis on the natural decay of $^{176}\text{Lu}$

F. G. A. Quarati,<sup>1,2</sup> G. Bollen,<sup>3,4,5</sup> P. Dorenbos,<sup>1</sup> M. Eibach,<sup>3,6</sup> K. Gulyuz,<sup>7</sup> A. Hamaker,<sup>3,5</sup> C. Izzo,<sup>3,5</sup> D. K. Keblbeck,<sup>7</sup> X. Mougeot,<sup>8</sup> D. Puentes,<sup>3,5</sup> M. Redshaw,<sup>3,7</sup> R. Ringle,<sup>3</sup> R. Sandler,<sup>7</sup> and I. Yandow<sup>3,5</sup>

<sup>1</sup>*AS, RST, LM, Delft University of Technology, Mekelweg 15, 2629JB Delft, The Netherlands*

<sup>2</sup>*Gonitec BV, Johannes Bildersstraat 43, 259EE Den Haag, The Netherlands\**

<sup>3</sup>*National Superconducting Cyclotron Laboratory, East Lansing, Michigan, 48824, USA*

<sup>4</sup>*Facility for Rare Isotope Beams, East Lansing, Michigan, 48824, USA*

<sup>5</sup>*Department of Physics and Astronomy, Michigan State University, East Lansing, Michigan 48824, USA*

<sup>6</sup>*Institut für Physik, Universität Greifswald, 17487 Greifswald, Germany*

<sup>7</sup>*Department of Physics, Central Michigan University, Mount Pleasant, Michigan, 48859, USA*

<sup>8</sup>*Université Paris-Saclay, CEA, List, Laboratoire National Henri Becquerel (LNE-LNHB), F-91120 Palaiseau, France*

(Dated: April 22, 2022)

**Background:** Mainly because of its long half-life and despite its scientific relevance, spectroscopic measurements of  $^{176}\text{Lu}$   $\beta$  decays are very limited and lack formulation of shape factors. Direct measurement of its Q-value is also presently unreported. In addition, the description of forbidden decays provides interesting challenges for nuclear theory. The comparison of precise experimental results with theoretical calculations for these decays can help to test underlying models and can aid the interpretation of data from other experiments.

**Purpose:** Perform the first precision measurement of  $^{176}\text{Lu}$   $\beta$ -decay spectrum and attempt the observation of its electron capture decays, as well as perform the first precision direct measurement of the  $^{176}\text{Lu}$   $\beta$ -decay Q-value. Compare the shape of the precisely determined experimental  $\beta$ -spectrum to theoretical calculations, and compare the end-point energy to that obtained from an independent Q-value measurement.

**Method:** The  $^{176}\text{Lu}$   $\beta$ -decay spectra and the search for electron capture decays were measured with an experimental set-up that employed lutetium-based scintillator crystals and an NaI(Tl) spectrometer for coincidence counting. The  $\beta$ -decay Q-value was determined via high-precision Penning trap mass spectrometry (PTMS) with the LEBIT facility at the National Superconducting Cyclotron Laboratory. The  $\beta$ -spectrum calculations were performed within the Fermi theory formalism with nuclear structure effects calculated using a shell model approach.

**Results:** Both beta transitions of  $^{176}\text{Lu}$  were experimentally observed and corresponding shape factors formulated in their entire energy ranges. Search for electron captures decay branches led to an experimental upper limit of  $6.3 \times 10^{-6}$  compared to its  $\beta$  decays. The  $^{176}\text{Lu}$   $\beta$ -decay and electron capture Q-values were measured using PTMS to be 1193.0(6) keV and 108.9(8) keV, respectively. This enabled precise  $\beta$  end-point energies of 596.2(6) keV and 195.3(6) keV for the primary and secondary  $\beta$ -decays, respectively, to be determined. The conserved vector current hypothesis was applied to calculate the relativistic vector matrix elements. The  $\beta$ -spectrum shape was shown to significantly depend on the Coulomb displacement energy and on the value of the axial vector coupling constant  $g_A$ , which was extracted according to different assumptions.

## I. INTRODUCTION

The primordial, long-lived,  $^{176}\text{Lu}$  radionuclide possesses unique relevance in nuclear astrophysics, nucleosynthesis, geo- and extraterrestrial-chronology [1–7] and additional relevance in nuclear structure science and applications [8–11].

The dominant transition of  $^{176}\text{Lu}$  (see Fig. 1) is a forbidden  $\beta$ -transition and the study and description of such types of  $\beta$ -decay has itself shown to provide both experimental and theoretical challenges along with more practical applications, as outlined in [12]. For instance, precise measurements and theoretical descriptions of  $\beta$ -spectra could provide a method to extract a value for the weak axial vector coupling constant,  $g_A$ , as recently described by Haaranen *et al.* [13]. Besides, these kinds of  $\beta$ -decays can create significant, sometimes dominant

background events in highly sensitive experiments, such as (neutrinoless) double  $\beta$ -decay, dark matter searches, and solar- and geo-neutrino experiments [14–16]. More specifically for  $^{176}\text{Lu}$ , recent developments have shown that precise knowledge of the  $\beta$ -spectrum shape is fundamental for a precise half-life determination by liquid scintillation counting [17–19]. Therefore, the availability of precise shape factors for  $^{176}\text{Lu}$  can enable a more accurate determination of its half-life, which is crucial for application of the Lu-Hf dating system in geochronology. Early investigations on the natural radioactivity of lutetium include the work of Heyden and Wefelmeier, and that of Libby, both in 1939 [20, 21]. Despite the numerous successive publications, the work of Dixon *et al.* in 1954 [22] and Prodi *et al.* in 1969 [23] remain the only available references for empirical  $\beta$  end point and  $\beta$ -spectrum shape for the dominant (>99%)  $\beta$ -transition of  $^{176}\text{Lu}$ . Both of them, however, made evaluations of the end point inconsistent with recent atomic mass evaluation data (AME2020) [24] and both observed  $\beta$ -spectra in good agreement with that expected for an allowed tran-

---

\* f.g.a.quarati@tudelft.nl

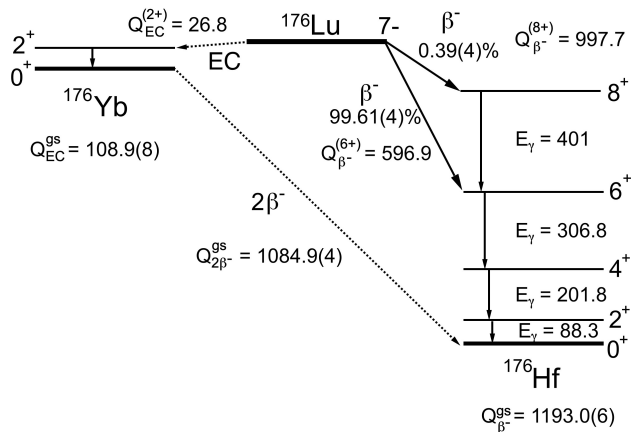


FIG. 1. Decay scheme for Lu-Hf-Yb  $A = 176$  triplet. Solid arrows indicate the observed 1<sup>st</sup> forbidden non-unique  $\beta$ -decays of  $^{176}\text{Lu}$ , and dotted arrows indicate the energetically allowed, but as yet unobserved 5<sup>th</sup> forbidden non-unique EC decay of  $^{176}\text{Lu}$ , and the double  $\beta$ -decay of  $^{176}\text{Yb}$ .

sition. Therefore, experimental  $\beta$ -shape factors for  $^{176}\text{Lu}$  are until now unavailable in the literature. Similarly, precise direct measurements of the  $Q$  value of  $^{176}\text{Lu}$  have not been previously reported; an experimental  $Q$  value was previously obtained by Ketelaer *et al.* [25] from individual Penning trap measurements of parent and daughter atomic masses, but with an uncertainty of  $\sim 11$  keV. Hence, a new direct measurement is called for.

As shown in Fig. 1,  $^{176}\text{Lu}$  decays via a 1<sup>st</sup> forbidden  $\beta$ -decay predominantly to the 6<sup>+</sup> state in  $^{176}\text{Hf}$ , and via a weaker decay branch to the 8<sup>+</sup> state, with a half-life of  $3.76(7) \times 10^{10}$  y [26]. Electron capture (EC) decay of  $^{176}\text{Lu}$  to  $^{176}\text{Yb}$  is also energetically allowed, but such a decay to the 2<sup>+</sup> state in  $^{176}\text{Yb}$  is 5<sup>th</sup> forbidden and modern decay experiments and geochemical tests have shown no indication of this decay branch [27–29].  $^{176}\text{Lu}$  is also the most strongly bound isotope in a nearly stable triplet, so double  $\beta$ -decay of  $^{176}\text{Yb} \rightarrow ^{176}\text{Hf}$  is also energetically allowed. Again, experimental searches for this decay have been performed, but it has not been observed [30].

We describe herewith our efforts to improve the knowledge of  $^{176}\text{Lu}$  decay, aiming at precise evaluations of the  $Q$ -values, the  $\beta$ -spectrum shapes, and their end-point energies. We also formulate much stricter limits for its EC branches. In addition, theoretical calculations of these  $\beta$ -decays and extensive comparisons of the results with our measurements have been performed. The current limits on the EC decay branches of  $^{176}\text{Lu}$  have been revised as well. The paper is organized as follows: in Sec. II A to II C, we describe in detail the precise measurement of the  $\beta$ -spectrum and its end-point energy for  $^{176}\text{Lu}$  decay using LSO:Ce and LuAG:Pr scintillators, including a brief reintroduction of the self-scintillation method. In Sec. II D, we report on the investigation of the EC decay of  $^{176}\text{Lu}$ . In Sec. III, we describe the first direct measurement of the  $^{176}\text{Lu}$   $\beta$ -decay  $Q$ -value via Penning trap mass spectrometry measurements of the mass ratio

of parent and daughter ions. The theoretical calculations of  $^{176}\text{Lu}$   $\beta$ -decay and subsequent analyses are depicted in Sec. IV. Finally, we summarize and discuss the results, their significance and envisaged implications in the last section.

## II. $\beta$ -SPECTRUM MEASUREMENTS

### A. The self-scintillation method for $^{176}\text{Lu}$

Spectroscopic  $\beta$ -decay measurements of long-lived nuclides such as  $^{176}\text{Lu}$  are challenging due to the low activity achieved by standard radioactive sources. A scintillator detector whose molecules contain the long-lived nuclide, either by natural occurrence or by means of doping, is particularly suitable to cope with this challenge. In this case, the radioactive source and the scintillator detector form a sort of calorimeter, and by means of pulse height spectroscopic measurements of the self-scintillation, alias intrinsic background, one can then detect the  $\beta$ -spectrum shape. Such self-scintillation methods were applied in the past and a notable example is the work of Beard and Kelly in 1961 [31]. More recently, we have applied the self-scintillation method to the measurement of the  $\beta$ -spectrum shape of  $^{138}\text{La}$  using LaBr<sub>3</sub>:Ce and CeBr<sub>3</sub> scintillators [32–34].

In the past three decades, achievements in research and engineering have made available numerous Lu-containing scintillators such as LSO:Ce, LuAP:Ce, LYSO:Ce, LuAG:Pr and LuYAP:Pr [35–39]. Because of their high density and fast response, these scintillators found their main applications in positron emission tomography.

The natural occurrence of  $^{176}\text{Lu}$  generates in these scintillators a specific activity ranging from 150 Bq/cm<sup>3</sup> up to 300 Bq/cm<sup>3</sup>, quite remarkable when compared to the over 30 billion year long half-life of  $^{176}\text{Lu}$ . Current research on the physics of the scintillation mechanism includes relevant experiments and data on the so called scintillation non-proportionality of the response (nPR), namely, the number of scintillation photons produced by  $\gamma$ - and  $\beta$ -ray interactions is not linearly proportional to the energy deposited in the scintillator [40]. The nPR particularly affects the energies below 100 keV and, thanks also to dedicated studies such as those of Payne *et al.* and Khodyuk and Dorenbos [41–43], it could be effectively taken into account in the present work.

As detailed in the following subsection, given the relative complexity of the  $\beta$ -decay branch of  $^{176}\text{Lu}$  (Fig. 1) with two transitions and four excited levels, there is not a straight-forward method for its spectroscopic measurements, but rather various possible configurations. This aspect is addressed in the next subsection.

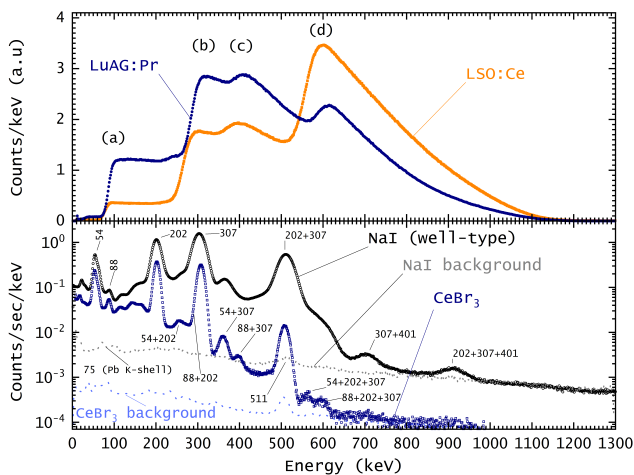


FIG. 2. Top, self-scintillation spectra of LuAG:Pr and LSO:Ce. Bottom, gamma-ray emission escaping LuAG:Pr and LSO:Ce and detected by NaI and CeBr<sub>3</sub> spectrometer. All measurements are performed inside a lead castle. All reported energy values are in keV.

## B. Experimental apparatus and methods

The self-scintillation spectra of two Lu-containing scintillators are reported in Fig. 2 (Top). The spectra were measured with LSO:Ce and LuAG:Pr scintillators with sizes of  $3.2 \times 3.2 \times 1 \text{ cm}^3$  ( $10.2 \text{ cm}^3$ ) and  $8 \times 8 \times 8 \text{ mm}^3$  ( $0.5 \text{ cm}^3$ ), respectively. The measurements were performed by coupling the scintillators to a photomultiplier tube (PMT) and placing the resulting assembly inside a low-activity lead-castle. Signal read out and acquisition involved widely available nuclear spectroscopy equipment such as a shaping amplifier and analog-to-digital converter of the NIM and CAMAC standard. Both spectra are dominated by the dominant  $\beta$ -transition (99.6% probability) of  $^{176}\text{Lu}$  and one can distinguish four main sawtooth-shaped peaks marked (a), (b), (c), and (d) in Fig. 2 (Top). With reference to the decay scheme of  $^{176}\text{Lu}$  (Fig. 1) these peaks can be identified by the possible combinations of true sum coincidence detection and escape of the three  $^{176}\text{Lu}$  de-excitation emissions of 88.34 keV, 201.83 keV and 306.78 keV and the  $\beta$  as follows: (a)  $88 + \beta$  (202 and 307 escape), (b)  $88 + 202 + \beta$  (307 escape), (c)  $88 + 307 + \beta$  (202 escape), (d)  $88 + 202 + 307 + \beta$  (no escape). Just above, as well as in the following text, the final state levels of the  $^{176}\text{Lu}$   $\beta$ -decay branch (Fig. 1) have been labeled using their energy rounded to the nearest 1 keV, i.e. 88, 202, 307, and 401.

The spectra of Fig. 2 (Top) also include some events from the minor (0.4% probability)  $\beta$  transition. If fully detected this should give rise to a fifth sawtooth-shape peak at 998 keV, which is not observed because of the large escape probability of the 401 keV even for the larger LSO:Ce scintillator. Therefore, most of the minor  $\beta$  transition related events overlap with that of the dominant transition, making it indistinguishable. Electron capture decay of  $^{176}\text{Lu}$  (see Fig. 1) are also potentially present in

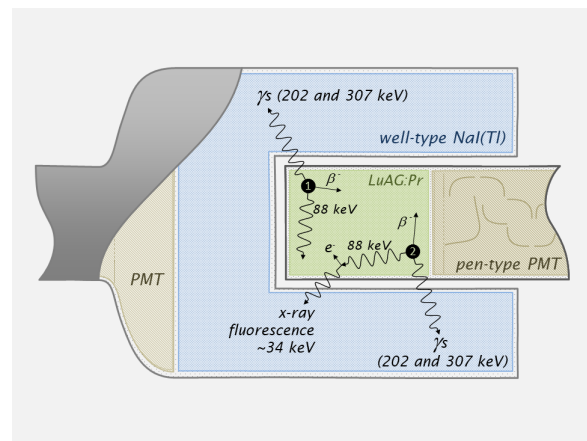


FIG. 3. The experimental setup:  $4\pi$  NaI.

the spectra of Fig. 2 (Top). However we could not observe any obviously related features. We report further on EC in the dedicated Section IID.

Another feature of both spectra in Fig. 2 (Top) is a much smaller sawtooth-shaped peak around 34 keV. This is related to the generation of K-shell fluorescence x-rays which, in turn, escapes the scintillator. The K-shell fluorescence is mainly that of Lu with an average energy of 54 keV, hence the position of the peak at  $88 - 54 = 34$  keV. One more notable feature is the relatively larger (d) peak observed with LSO:Ce. This is simply due to its much larger size and hence larger detection efficiency at 307 keV.

Effects of scintillation non-proportionality of the response (nPR), see e.g. [40–43] are also observable in Fig. 2 (Top). In fact, the spectra are linearly calibrated from channel to energy by taking into account the nPR characteristic of each scintillator. For instance, LSO:Ce nPR at 60 keV is of the order of 83%, hence we calibrate the  $^{241}\text{Am}$  main peak at  $59.54 \times 0.83 = 49.4$  keV. For comparison, LuAG:Pr nPR at 60 keV is 97%. As a consequence of this calibration one can observe that the middle of the left edge of peak (a) is found approximately at 76 keV for LSO:Ce and at 87 keV for LuAG:Pr, both in agreement with their specific nPRs (86% and 98% respectively). The advantage of such a calibration is to preserve the actual response of the scintillator that can then be taken into account at a later stage in the construction of the response function. For further information specifically concerning the escape probabilities of the various emissions in the case of LSO:Ce and LYSO:Ce, to some extent applicable as well to nearly equally dense LuAG:Pr, we refer to the dedicated work of Alva-Sánchez *et al.* [44].

A detailed analysis of the above self-scintillation spectra could lead to some capability of extracting the true  $\beta$ -spectrum of the dominant  $\beta$ -transition of  $^{176}\text{Lu}$ . However, the presence of the minor  $\beta$ -transition distorts to a certain degree the shape of the  $\beta$ -spectrum at energy below 200 keV. Therefore one would need to make some assumptions on both  $\beta$  shapes in order to disentangle each

contribution from the other, discouraging one to proceed in this direction. Nonetheless we have further analyzed the self-scintillation as reported below in Section II C

The bottom part of Fig. 2 reports the emission of a  $1 \text{ cm}^3$  LuAG:Pr scintillator as detected by a well-type  $3'' \times 6''$  NaI spectrometer ( $4\pi$  geometry) and a  $2'' \times 2''$  CeBr<sub>3</sub> spectrometer ( $<2\pi$  geometry). Again, the measurements were performed inside a lead-castle and the residual environmental activity is also reported as the background spectrum for both NaI and CeBr<sub>3</sub> spectrometers. From the spectra it can be noted that the 88 keV gamma ray has a low probability to escape from the scintillator, not only because it interacts within the scintillators rather than escaping, but also because of its original low emission intensity of 14.5%. Alva-Sánchez *et al.* evaluated its escape probability from a  $1 \text{ cm}^3$  LYSO:Ce scintillator as 5.1% [44]. Therefore, triggering the escape of the whole de-excitation cascade of 88+202+307 keV to observe solely the corresponding  $\beta$  in the scintillator will lead to a severe loss of counting efficiency that cannot be compensated for by simply increasing the size of the scintillator. Moreover, the limited energy resolution of the NaI (8.5% FWHM at 662 keV) makes the 88+202+307 keV peak poorly resolved from those of 202+307 keV and 54+202+307 keV. This is not the case for the CeBr<sub>3</sub> (4% FWHM at 662 keV), which can resolve all three peaks. Nevertheless, by comparing the counting efficiency of the two spectra with NaI and CeBr<sub>3</sub>, the advantage of a  $4\pi$  geometry became evident. For the 202+307 keV peak, the counting efficiency increases at least 8 fold using a  $4\pi$  instead of a  $<2\pi$  geometry.

Another aspect to be considered is that, with typical densities around  $7 \text{ g/cm}^3$ , Lu-containing scintillators strongly attenuate  $\gamma$ -rays. Therefore, according to NIST XCOM [45], a limit of about  $1 \text{ cm}^3$  in the dimensions of the Lu-containing scintillator exists to allow about 20% of the 307+202 keV emissions to escape the scintillator.

Combining all of the above observations, the setup for the  $\beta$ -spectroscopy measurements has been designed to use the well-type NaI(Tl) spectrometer with a Lu-based scintillator inside its well, coupled to a pen-type PMT as schematically shown in Fig. 3. Every time that the NaI(Tl) detects 307+202 keV, the Lu-based scintillator detects the  $\beta$  in coincidence with the 88 keV emission. As a consequence, the  $\beta$  detection is offset by and convolved with the 88 keV emission. This makes the use of a Lu-based scintillator with satisfactory response in terms of energy resolution and proportionality crucial in order to reduce as much as possible the corresponding spectral smear. Unfortunately, the size of the NaI(Tl) well of  $2/3''$  (1.69 cm) diameter implies the use of a  $\varnothing 13 \text{ mm}$  pen-type PMT, which typically offers modest quantum efficiency on the order of 20%.

In the end, we selected LuAG:Pr scintillators for the spectroscopic measurements of  $^{176}\text{Lu}$   $\beta$ -decay. LuAG:Pr stands for Lutetium Aluminum Garnet doped with Praseodymium ( $\text{Lu}_3\text{Al}_5\text{O}_{12}:\text{Pr}$ ). It has density of  $6.7 \text{ g/cm}^3$  and an achievable energy resolution  $<5\%$  FWHM at 662 keV. Its response is about 93% proportional at

10 keV, and its specific activity is  $215 \text{ Bq/cm}^3$ . In comparison, LSO:Ce (Lutetium Oxyorthosilicate doped with Cerium,  $\text{Lu}_2\text{SiO}_5:\text{Ce}$ ) has a density of  $7.4 \text{ g/cm}^3$ , energy resolution of about 8% FWHM at 662 keV, 65% response proportionality at 10 keV, and  $295 \text{ Bq/cm}^3$  of specific activity. Custom sizes of LuAG:Pr were procured from Kinheng [46] and a demountable pen-type PMT assembly from Scionix [47]. The energy resolution actually achieved with LuAG:Pr and the pen-type PMT was eventually 8% FWHM at 662 keV.

With the setup represented in Fig. 3, we acquired the self-scintillation with a  $8 \times 8 \times 8 \text{ mm}^3$  LuAG:Pr scintillator in coincidence with the well-type NaI(Tl) detecting 202+307 keV. The measurement lasted for nearly 10 days and, with a counting rate of about 10 cps,  $8.5 \text{ M}$   $\beta$ -decays were recorded. The stability of the signal against temperature and gain drifts was measured and showed limited fluctuations of less than 0.15%. The raw  $^{176}\text{Lu}$   $\beta$ -spectrum is shown in Fig. 4. As mentioned earlier, this spectrum is not purely a  $\beta$ -spectrum but the convolution of the  $\beta$  with the  $^{176}\text{Hf}$  de-excitation emission of 88 keV. This last is detected by LuAG:Pr with an energy resolution of 24% FWHM, equivalent to  $\sigma = 9 \text{ keV}$ .

As in the self-scintillation spectra of Fig. 2, one can again observe the small sawtooth-shaped/step-like peak at 34 keV due to fluorescence emissions. As schematically reported in the setup of Fig. 3, the 88 keV gamma-ray can generate a fluorescence x-ray which in turn can escape the scintillator. Even with the limited energy resolution of the NaI(Tl) (see the overlap of the 202+307 keV and 54+202+307 keV peak in Fig. 2) one could set the gate to trigger out these unwanted events. However, they cannot be totally suppressed. In fact the 54 keV fluorescence can also be absorbed in the dead layers surrounding the detectors, mostly aluminum, with equivalent consequences. Therefore, we instead triggered out almost entirely the 202+307 keV by setting the gate on the 54+202+307 keV and measured a spectrum dominated by fluorescence +  $\beta$  which is shown in Fig. 4. This spectrum can be subtracted from the 88 keV +  $\beta$  in order to remove the unwanted events.

Besides the above, we also measured the second, least probable,  $\beta$ -transition of  $^{176}\text{Lu}$  and the raw data are reported in Fig. 5. This measurement was analogous to that of the first  $\beta$ -transition but with the gate set to trigger the 202+307+401 keV cascade. Here the count rate achieved was only 1.7 counts per minute and the acquisition had to last over one month to collect 83000 counts. A more severe gain drift with a drop approaching 1% was observed in the last week of the acquisition, quite possibly because of a change in the laboratory temperature, and we have corrected for it. Also, because of the low counting efficiency, this time the background due to the fluorescence related events was not measured but rather synthetically simulated based on the expected shape of the  $\beta$ -transition. This synthetic background is also reported in Fig. 5.

Another important measurement was performed with the setup of Fig. 3 with two pairs of LuAG:Pr scintilla-

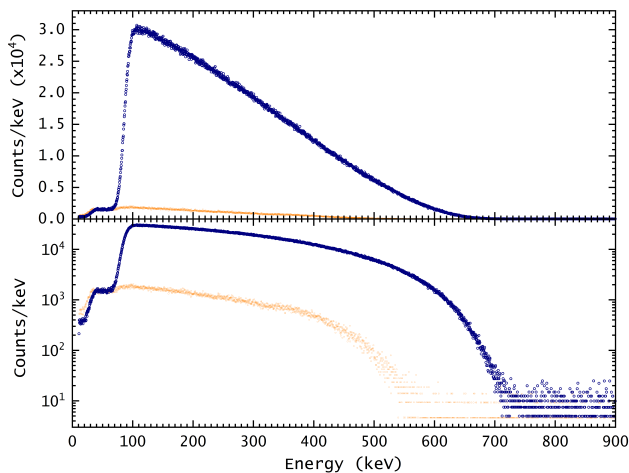


FIG. 4. The raw spectrum of the first  $^{176}\text{Lu}$   $\beta$ -transition (blue) and the measured background (yellow), see text for details.

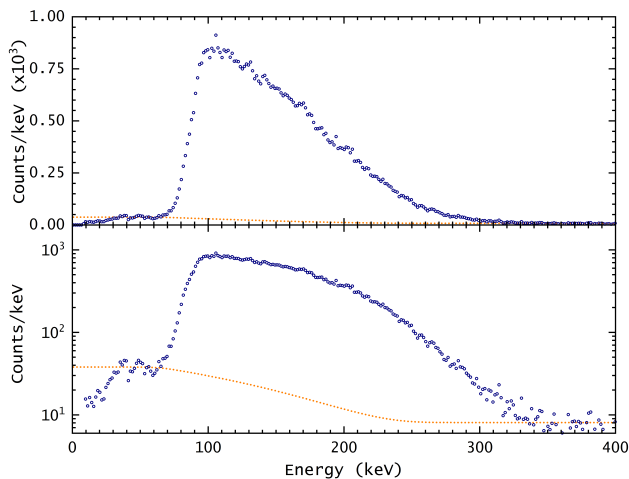


FIG. 5. The raw spectrum of the second  $^{176}\text{Lu}$   $\beta$ -transition (blue) and the synthetically simulated background (yellow), see text for details.

tors:  $8 \times 8 \times 2 \text{ mm}^3$  and  $8 \times 8 \times 8 \text{ mm}^3$  cubic samples, and  $\emptyset 10 \times 2 \text{ mm}^3$  and  $\emptyset 10 \times 10 \text{ mm}^3$  cylindrical samples, with the aim to observe small detector effects [48]. These effects occur when the  $\beta$  escapes the scintillator and only part of its energy is detected causing a migration of counts from higher energy to lower energy in the shape of the  $\beta$ -spectrum. Despite the fact that the smaller samples have thicknesses about just twice the range of a 600 keV  $\beta$  in LuAG:Pr, as shown in Fig. 6, each pair of spectra nicely overlap along the whole energy range. This result is further discussed in Sec. II C along with the implementation of the experimental response function.

### C. $^{176}\text{Lu}$ $\beta$ -spectrum measurement results

In order to analyze the measured spectra we proceed by implementing the response function applicable to our experiment. We identified three sources of spectral spread, namely: i) finite energy resolution, ii) non-proportionality of the response (nPR) and, iii), small detector effects. In addition, the  $\beta$  particles have been measured in coincidence with 88 keV de-excitation emission. Therefore, the two signatures must be separated as well.

As explained above there were constraints on the maximum volume of the scintillator, hence we were particularly concerned by small detector effects. To evaluate them we used a fully empirical approach which eventually led to consider negligible that source of distortion in the present experiment.

Small detector effects can be expected for  $\beta$  particles emitted in close proximity to the surface of the scintillator that, as such, are more likely to escape the detector volume and hence avoid full energy deposition inside the scintillator. Moreover, during the process of slowing down to rest,  $\beta$  particles can also emit bremsstrahlung radiation that, again, might escape the scintillator volume and hence detection. Since the higher the  $\beta$  energy, the higher are both escape probabilities mentioned above, it can be expected that small detector effects appear in a  $\beta$  spectrum as a migration of counts from the higher and middle energy channels to the lower energy channels.

According to NIST ESTAR [49], for LuAG:Pr one expects a range of about 0.5 mm for 600 keV  $\beta$  particles, this in the continuous slowing down approximation (CSDA). Although this is just an approximation of the actual path of an electron, advanced simulations generally appear in good agreement with it, as in the case of Prange *et al.* [50]. Now, the thickness of the smaller

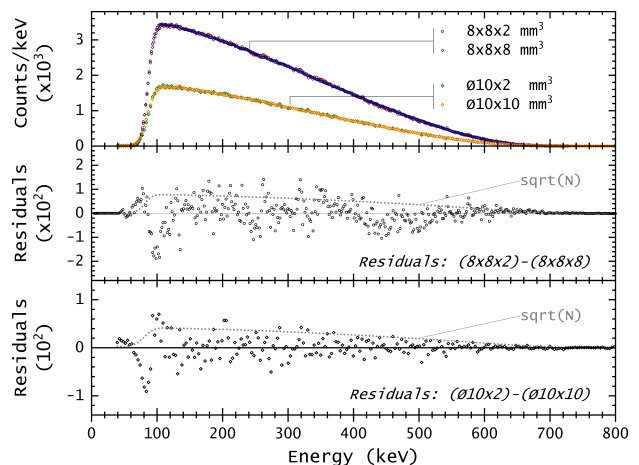


FIG. 6. Comparison of  $\beta$ -spectrum detected with two samples of LuAG:Pr of different dimensions, i.e.  $8 \times 8 \times 8$  and  $8 \times 8 \times 2$ . Top: the normalised spectra. Bottom: the residuals after their subtraction. The residuals are tested by a orthogonal distance regression to observe possible small detector effects.

LuAG:Pr scintillators is 2 mm and therefore, considering the 0.5 mm electron range, about half of their volume is potentially affected by small detector effects. However not even a minor migration of counts could be observed by comparing the  $\beta$  spectrum measured with it to the ones measured with the larger 8-mm-thickness-scintillators as shown in Fig. 6.

The initial idea was to measure several scintillators with increasing thickness in order to quantify small detector effects vs the size of the scintillators, extrapolate the response of an ideally unaffected scintillator and then evaluate the correction for a real one. Substantial small detector effects were not expected based on previous experience with  $^{138}\text{La}$  as well as with experience in characterization of small scintillators in the frame of materials research (e.g. [51]), however the lack of any distinguishable effects was not anticipated for a dedicated experiment.

Such a lack of effects is rational for what concerns the bremsstrahlung. In fact, below 1 MeV, the energy loss of  $\beta$  particles is dominated by collision processes rather than by bremsstrahlung emission and, according to NIST XCOM [45], one expects the radiation yield of a 600 keV  $\beta$  to be of the order of 1% with an energy of about 17 keV. In turn, an x-ray of 17 keV has 99% absorption probability within 0.1 mm of LuAG:Pr and hence its overall escape probability becomes marginal.

Concerning the  $\beta$  escapes, we could not find in the literature any equivalent experiment and so we could not compare our results with that of others. We consider all the above a quite interesting topic for further empirical and simulation-based investigations. On the one hand, it is rational to expect that a certain scintillator material presents a sort of minimum critical volume that can no longer absorb all  $\beta$  particles and their energy, hence causing distinguishable effects in the shape of the  $\beta$ -spectrum. On the other hand, we can conclude that that volume must be substantially smaller compared to the  $\beta$  range and, therefore, in the context of the present experiment, no small detector effects need to be accounted for.

The response function was implemented taking into account the finite energy resolution and the nPR. The energy resolution as a function of energy of LuAG:Pr coupled with the low QE pen-PMT can be well represented by  $\sigma = 0.93E^{-0.50}$  with  $E$  expressed in keV. With a standard PMT we measured  $\sigma = 0.43E^{-0.51}$ , leaving a margin for further improvements. For each  $\beta$  decay, both the corresponding  $\beta$  and 88 keV de-excitation emission are coincidentally measured. However they follow distinct, uncorrelated scintillation processes and hence their energy resolutions combine in quadrature. With a  $\sigma$  of about 9 keV, the energy resolution of 88 keV emission dominates the lower energy part of the spectrum.

Data on nPR of LuAG:Pr are available from [41–43] covering, respectively, the energy range above 10 keV and below 100 keV. The two curves present some discrepancy and we averaged the two into a smooth s-shaped curve. As further discussed later on, for the present experiment the effects of nPR are reduced/washed out by

the relatively large energy resolution of the 88 keV emission. Therefore, even a moderate misestimation of nPR leads to no observable effects in the measured  $\beta$ -spectrum shape. However, as further discussed below, it is also the true value of the nPR at 88 keV that determines the spread of the measured  $\beta$  spectrum at the lower energies.

The effects of nPR can be observed by comparing the  $\beta$ -spectra collected with LuAG:Pr and with LSO:Ce, shown in Fig. 7 (Top). Because of the pen-type PMT used for LuAG:Pr, the energy resolution of the two scintillators are nearly equivalent. However, their spectra present two main differences both due to nPR effects. First of all, the LSO:Ce spectrum starts at lower energies than that of LuAG:Pr because of its stronger nPR which makes the detection of the 88 keV emission occur at 76 keV. Secondly, the peak's top of the LSO:Ce spectrum appears sharper than that of LuAG:Pr again because of its stronger nPR which generate an accumulation of counts at the lower  $\beta$  energies.

The response function was implemented in the form of a discrete matrix which generates the probability distribution to observe a  $\beta$  with true energy  $E$  at energy  $E'$  in the measured spectrum. We firstly applied the response function to the allowed  $\beta$ -spectrum of  $^{176}\text{Lu}$  (i.e.  $C(W)=1$ ) and the results are shown in Fig. 7 (Bottom) for the response functions of both LuAG:Pr and LSO:Ce. It can be observed that, in the case of LuAG:Pr, from 110 keV in the experiment scale (which corresponds to  $110 - (88 \times nPR) \approx 22.5$  keV in the  $\beta$  spectrum) the folded spectrum basically overlaps the unfolded one. The same does not occur for LSO:Ce for which, in reason of its stronger nPR, one can observe the mentioned accumulation of counts at the lower energies affecting its top. Moreover, one can also observe that, as the LSO:Ce  $\beta$ -spectrum is smeared down to lower energies compared to that of LuAG:Pr, again due to its stronger nPR, the 88

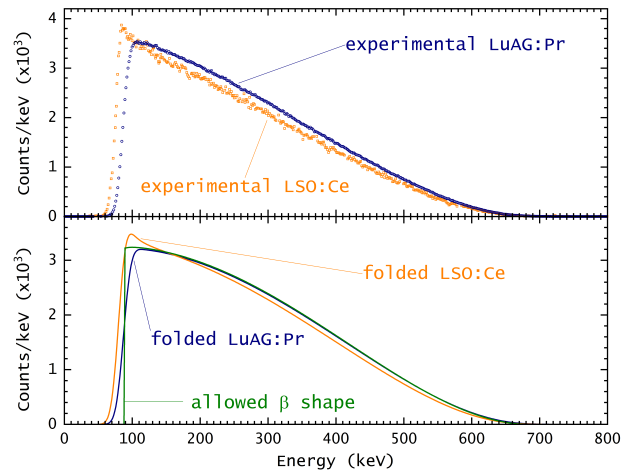


FIG. 7. Top: Effect of nPR as seen in two spectra of  $^{176}\text{Lu}$ , one measured by “proportional” LuAG:Pr and another measured by non-proportional LSO:Ce. Bottom: Implementation of the response matrix, which can be seen to reproduce the nPR effect of both scintillators.

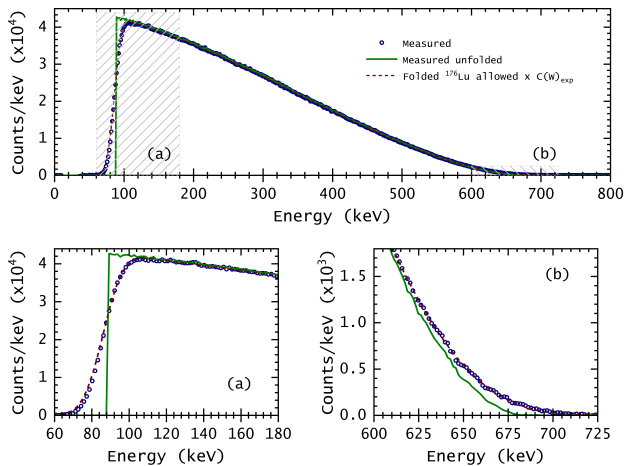


FIG. 8. The  $^{176}\text{Lu}$  spectra measured by LuAG:Pr and unfolded using the response function. As seen the distortions due to mostly finite energy resolution in the case of LuAG:Pr occur in the first 20 keV and toward the end point.

keV emission is subsequently detected at 76 keV.

The response function was then used to unfold the measured  $\beta$ -spectrum into an approximation of the true spectrum by an iterative procedure. As mentioned earlier, the first 20 keV of the measured  $\beta$ -spectrum (i.e. the region from 88 keV to 88+20 keV) is offset and spread by the 88 keV of the de-excitation emission, with its nPR and its energy resolution  $\sigma = 9$  keV. The unfolding of this region of the spectrum presented a notable aspect. In fact, we found that uncertainties in the actual nPR at 88 keV have noticeable effects in the shape of the first 20 keV of the measured  $\beta$ -spectrum. In other words, the true nPR at 88 keV plays a crucial role and needs careful re-evaluation during the unfolding procedure. Note that uncertainties in the nPR at 88 keV do not directly propagate to the end point since there, that energy is summed to the energy of the  $\beta$ , and the resulting nPR becomes negligible. We found that the measured spectrum can be reproduced by re-folding the unfolded one if, in reason of the nPR, the 88 keV corresponds to 87 keV, consistently with the available data. For the unfolding procedure we applied the algorithm by Wortman and Cramer [52] and the results are reported in Fig. 8. The unfolded spectrum can be considered a robust approximation of the true one from 88+20 keV to the end point as confirmed also by testing with different unfolding algorithms such as the one by Magain [53]. The shape of the first 20 keV of the unfolded spectrum is, however, less robust and presents up to 3% relative uncertainty in its first 3 keV.

For an independent evaluation of the experimental end point of the main  $\beta$  transition observed with LuAG:Pr, we lacked readily available shape factors and proceeded as follows. The unfolded experimental spectrum of Fig. 8, with its energy scale corrected for the offset produced by the 88 keV emission, was used together with a set of nine allowed  $\beta$ -spectra whose end points were increased from 591.0 keV up to 603.0 keV in steps of 1.5 keV. These

TABLE I. Results of the procedure to determine the experimental end point of the first  $\beta$  transition of  $^{176}\text{Lu}$  from its spectrum as measured by LuAG:Pr

Nominal end point (keV)	Fit end point (keV)	DoF	$\chi^2/\text{DoF}$ ( $\times 10^{-5}$ )
591.0	591.73(15)	392	2.42
592.5	593.11(14)	393	2.14
594.0	594.49(13)	394	1.92
595.5	595.86(13)	395	1.79
597.0	597.23(13)	396	1.74
598.5	598.56(13)	397	1.80
600.0	599.90(14)	398	1.98
601.5	601.24(15)	399	2.29
603.0	602.58(16)	400	2.72

spectra were obtained using BetaShape software [54, 55] and the end point values were chosen to cover a 12 keV range around the end point value of 597.0 keV derived from [24]. For each spectrum in the set of nine, we evaluated the corresponding experimental shape factors in the form

$$C(W)_{exp} = \frac{(dN/dW)_{exp}}{(dN/dW)_{comp}} \quad (1)$$

$$= c(1 + aW + b/W + dW^2 + e/W^2)$$

where  $C(W)_{exp}$  denotes the experimental shape factors,  $W$  the total energy of the  $\beta$  particle including its rest mass,  $W = 1 + E/m_e$ ,  $(dN/dW)_{exp}$  the experimental spectrum,  $(dN/dW)_{comp}$  the computational spectrum for the allowed transition and  $c$ ,  $a$ ,  $b$ ,  $d$  and  $e$  the fitting parameters. The form of  $C(W)_{exp}$  was chosen to be able to fit the experimental shape factors corresponding to the most extreme end point values in the set of nine. We then proceeded by evaluating nine Kurie plots and fit them with straight lines. The results are reported in Table I. The experimental end point can now be evaluated in terms of the Kurie plot among the nine which present the minimum  $\chi^2/\text{DoF}$ . With reference to Table I, by plotting the  $\chi^2/\text{DoF}$  vs the nominal end points and fitting it with a parabola, a minimum is found and hence the end point is evaluated at 596.6(9) keV, well in agreement with the end point value obtained from the experimental  $Q$  value measured by the Penning trap technique (See section III B, Table VI).

An equivalent unfolding and end point evaluation procedure was applied to the second  $\beta$  transition. Here the set of nine allowed  $\beta$ -spectra ranged from 190.0 keV to 202.0 keV again in steps of 1.5 keV and the shape factors did not include the term  $e/W^2$ . The results are reported in Table II. Again by plotting the  $\chi^2/\text{DoF}$  vs the nominal end points and fitting it with a parabola, the value for the end point is found at 195.7(2.5) keV, once more in agreement with the end point value obtained from the experimental  $Q$  value (See section III B, Table VI).

Once the consistency of the end point values obtained by  $\beta$ -spectroscopy and from the Penning trap  $Q$  value



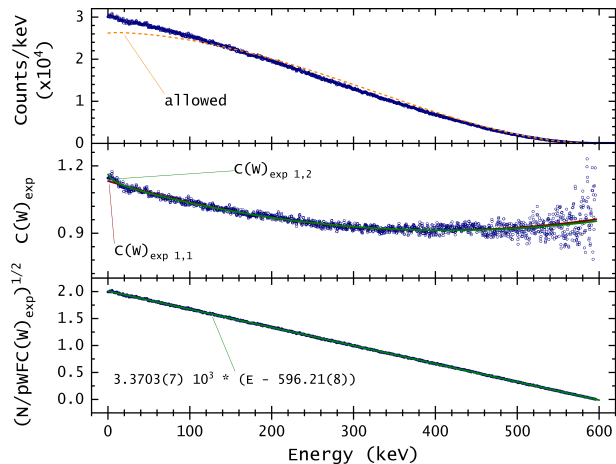


FIG. 9. The unfolded spectrum of the first  $\beta$  transition of  $^{176}\text{Lu}$ , the corresponding experimental shape factors and Kurie plot.

measurement was established, the latter values were taken to determine simpler forms of the shape factors because of their smaller uncertainty. For the first  $\beta$  transition this was done using a spectrum with bin width of 0.3 keV while for the second transition we used again a 1.5 keV bin width. The results are shown in Fig. 9 and Fig. 10. The shape factors of the first  $\beta$  transition are fitted by the parabolic equation in the form of  $C(W)_{exp\ 1,1} = 2.032(8) (1 - 0.615(5)W + 0.178(9)W^2)$ .

This equation however deviated from the experimental shape factors at energies below 10 keV. In order to cover that range a two parameter rational term can be added, and the obtained best fit becomes  $C(W)_{exp\ 1,2} = 1.967(11) (1 - 0.592(5)W + 0.163(2)W^2 + (1.6(8)10^{-5})/(1.029(9)W - 1)^2)$ . The best fit of the corresponding Kurie plot matches the expected end point of 596.21(8) keV

The shape factors of the second  $\beta$  transition are also fitted by the parabolic equation of  $C(W)_{exp\ 2,1} =$

TABLE II. Results of the procedure to determine the experimental end point of the second  $\beta$  transition of  $^{176}\text{Lu}$  from its spectrum as measured by LuAG:Pr

Nominal end point (keV)	Fit end point (keV)	DoF	$\chi^2/\text{DoF}$ ( $\times 10^{-4}$ )
190.0	191.0(5)	118	8.10
191.5	192.4(5)	119	7.66
193.0	194.0(5)	120	7.59
194.5	195.5(5)	121	7.42
196.0	197.1(5)	122	7.48
197.5	198.7(5)	123	7.68
199.0	200.3(5)	124	7.72
200.5	201.8(5)	125	7.86
202.0	203.4(6)	126	8.02

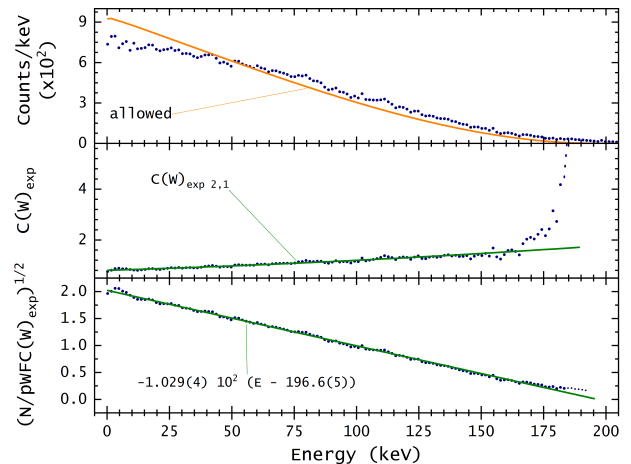


FIG. 10. The unfolded spectrum of the second  $\beta$  transition of  $^{176}\text{Lu}$ , the corresponding experimental shape factors and Kurie plot.

1.81(89)  $(1 - 1.95(9)W + 1.4(3)W^2)$ . As seen in Fig. 10, towards the end point the experimental shape factors are steeply growing and the equation does not follow that behaviour. However, given the rather modest counting statistics in the measured spectrum we desisted from further analysis. The best fit of the Kurie plot provided an end point value of 196.6(5) keV.

#### D. Evaluation of $^{176}\text{Lu}$ electron capture decay

As seen in Fig. 1, with a Q value of 108.9(8) keV (shortened to 109 keV in the text), there are two energetically allowed electron capture (EC) decays of  $^{176}\text{Lu}$  to  $^{176}\text{Yb}$ . One is a 5<sup>th</sup> forbidden non-unique transition to the 2<sup>+</sup>, 82.135(15) keV state of  $^{176}\text{Yb}$  (82 keV in the text). The second is a 7<sup>th</sup> forbidden non-unique transition to the 0<sup>+</sup> ground state of  $^{176}\text{Yb}$ ; both decays remain experimentally unobserved [27–29]. According to the limits by Norman *et al.* [27], the ratios of EC decay to  $\beta$ -decay are <0.45% and <0.36% for the 5<sup>th</sup> and 7<sup>th</sup> forbidden transition, respectively. Note that such limits compare to the <0.4% of the presently observed minor  $\beta$  transition of  $^{176}\text{Lu}$ .

As observed in previous studies of  $^{138}\text{La}$  [32, 33], EC decays in self-scintillation spectra appear as peaks centered at the binding energies of the captured electrons in the daughter nucleus and with areas proportional to the respective capture probabilities. The energy at which the peaks are observed can be offset by de-excitation emissions, as it is in the case of  $^{176}\text{Lu}$  to  $^{176}\text{Yb}(2^+, 82\text{ keV})$ . Capture probabilities of  $^{176}\text{Lu}$  are reported in Table III. They have been determined with the LogFT code [56] and the BetaShape code [55, 57]. None of them include the nuclear structure information that is required for these forbidden non-unique transitions. LogFT treats them as allowed while BetaShape treats them as forbidden unique transitions with the same change in total an-

gular momentum (i.e. as 4<sup>th</sup> and 6<sup>th</sup> forbidden unique, respectively), which mainly explains the different capture probabilities.

As mentioned in Section II B, the self-scintillation spectra of Fig. 2 (Top) would include counts originating from the EC decay branches of <sup>176</sup>Lu. These spectra are in fact collected without specific coincidence conditions, hence all EC decays can accumulate there along with the  $\beta$  decays. On the other hand, the raw  $\beta$  spectrum in Fig. 4 (as well as the one in Fig. 5) is virtually free from any EC decay event since the coincidence condition set for its acquisition, as described in Section II B, allows collection of EC related counts only as random coincidences. In turn, these are so unlikely that they can be neglected. In fact, thanks to the large signal-to-noise ratio used to generate the gate (which also lasts just 6  $\mu$ s), during that  $8.3 \times 10^5$  s long acquisition only about 20 s were actually available for the random coincidence, so that even with an over-exaggerated EC branching of 10% the amount of possible random coincidences is less than five counts. In other words, the self-scintillation spectrum and the raw  $\beta$  spectrum can be considered two extreme cases of, respectively, the presence of all possible EC counts and virtually no presence of EC counts.

Fig. 11 (Top) reports the first 130 keV energy range of both the raw  $\beta$  spectrum (same data as Fig. 4) and a self-scintillation spectrum which, below 130 keV, presents approximately the same number of counts of the  $\beta$  spectrum, i.e. 1.45 M. No obvious shape difference can be observed between the two spectra. Moreover, by normalizing the areas of the two in order to take into account the different contribution of the fluorescence escapes discussed in II B, residual analysis shows no statistically significant differences between their shapes. It is only above 110 keV (incidentally just above to EC Q-value) that the raw  $\beta$  spectrum start to deviate from the self-scintillation one, as dictated by its sawtooth-shaped  $88+\beta$  peak discussed in II B.

Fig. 11 (Top) reports as well the expected peaks for the two <sup>176</sup>Lu EC decay branches as would be detected by the  $8 \times 8 \times 8$  mm<sup>3</sup> LuAG:Pr, i.e. taking into account its energy resolution and nPR. Note that because of the Q value of 109 keV and the 82 keV of the 2<sup>+</sup> level, K-

TABLE III. Theoretical capture probabilities per electronic shell for <sup>176</sup>Lu decay. The associated energy as detectable in the LuAG:Pr is also reported (in keV).

	K	L	M	N	O	P
<hr/> <sup>176</sup> Lu(7 <sup>-</sup> , gs) $\rightarrow$ <sup>176</sup> Yb(2 <sup>+</sup> , 82.135(15) keV) <hr/>						
LogFT	0	0.508	0.492	-	-	-
BetaShape	0	0.0022	0.634	0.362	0.0013	3.3e-07
Energy	143.4	91.9	84.0	82.3	82.1	82.1
<hr/> <sup>176</sup> Lu(7 <sup>-</sup> , gs) $\rightarrow$ <sup>176</sup> Yb(0 <sup>+</sup> , gs) <hr/>						
LogFT	0.532	0.347	0.1215	-	-	-
BetaShape	1.43e-06	0.3068	0.5256	0.1616	0.00593	1.86e-06
Energy	61.3	9.8	1.9	0.2	0.04	0.01

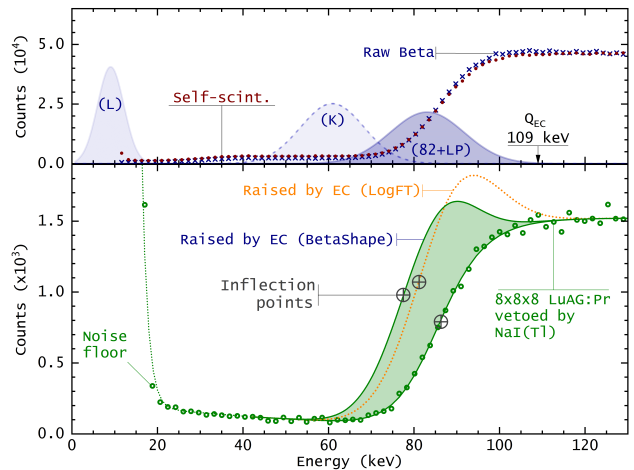


FIG. 11. LuAG:Pr spectra below 130 keV used for the search of EC decays. Top. Raw  $\beta$  and self-scintillation spectra (same spectra that in Fig. 2 and Fig. 4 respectively) and the expected EC peaks: (K-LP) all EC to the 82 keV level; (K) K-shell captures to the ground state; (L) L-shell captures to the ground state. Bottom. The self scintillation of LuAG:Pr collected in anti-coincidence with the NaI(Tl) and the effects corresponding to the detection of 10 k EC decays to the 82 keV level and for the capture probabilities of both BetaShape and LogFT.

shell captures are not considered since they violate energy conservation. The other energetically feasible electron captures of this branch, namely L-shell and higher shells up to the P-shell, have binding energies comparable or much smaller than the energy resolution of the LuAG:Pr with the pen-type PMT ( $\sigma = 8.5$  keV at 82 keV) hence all EC to the excited level merge into the single, bell like, broad peak labelled (82+LP) in Fig. 11 (Top). The figure also shows that the present LuAG:Pr set up can observe EC to the ground state only through the K-shell peak, since the peaks of the L-shell and higher shell fall behind the 10 keV acquisition threshold.

Each of the three EC peaks in Fig. 11 (Top) is normalized to about 300k counts, that roughly corresponds to the counts expected in the self-scintillation spectrum using the branching upper limits by Norman *et al.* [27]. For the K-shell peak, 300k counts is a gross over-estimation, being that the corresponding capture probability according to BetaShape very small (see Table III). On the contrary, the peak of the EC decays to the 82 keV excited level is a convolution of all possible shell captures and only marginally affected by their actual probabilities. As seen, the 82+LP peak overlaps with the left-edge of the  $88+\beta$  peak. By fitting the energy range between 60 keV and 110 keV of both the self-scintillation and the raw  $\beta$  spectra using a sigmoidal function, one can then look at the function inflection points to reveal the presence of EC to the 82 keV level. The value found for the inflection points are 86.28(5) keV and 86.16(4) keV for the self-scintillation and the raw  $\beta$  spectra respectively. The presence of EC would have shifted the inflection point of

the self scintillation to lower energy, the reverse of the above, hence the 0.12 keV observed difference cannot be considered significant for EC detection and rather arises from systematic uncertainties related to, e.g., energy calibration or gain stability ( $\pm 0.5\%$ ). Observation of EC decays cannot be claimed.

To search further for EC decays, a dedicated acquisition in anti-coincidence was carried out, again with the set up of Fig. 3. This time LuAG:Pr counts were vetoed when coincident counts in the NaI(Tl) were present. At energies below 130 keV, such acquisition provided a  $\beta$  self-scintillation spectrum dramatically reduced by nearly 70 times, hence substantially increasing the signal to noise ratio in favor of EC detection. Note that, on the whole energy range up to 1.2 MeV, the count rate in LuAG:Pr decreased only to about 1/3, consistent with its high detection efficiency. The LuAG:Pr spectrum vetoed by NaI(Tl) is reported in Fig. 11 (Bottom). Fitted again with a sigmoidal function, an inflection point of 86.2(2) keV was found, consistent with the fit values previously obtained, and characterised by a larger error because of its lower statistics, despite its acquisition lasting 0.61 Ms (170 hours) and collecting 19.2 M counts. One can logically conclude that even in the vetoed spectrum, the amount of possible EC captures is so marginal that it cannot emerge above statistical noise.

Note that the lack of EC detection cannot be associated to a lack of detection efficiency for the 82 keV. According to Ott *et al.* [28], its photon emission probability is in fact 0.125, close to that of the 88 keV level of  $^{176}\text{Hf}$  (i.e. 0.149). Due to this small emission probability, adapting the work of Alva-Sánchez *et al.* [44] to the present  $8 \times 8 \times 8 \text{ mm}^3$  LuAG:Pr, and reasonably assuming full efficiency for internal conversions, the detection efficiency of the 82 keV level is close to 100%. The actual evaluation led to 99.2%. Considering that each EC decay to the 82 keV level is detected introduces only a marginal uncertainty.

Fig. 11 (Bottom) shows as well the expected effect of 10k counts of EC decay to 82 keV level superimposed to the vetoed spectrum, this for both EC probabilities of BetaShape and LogFT (Table III). As seen, these 10k counts would have obviously deformed the vetoed spectrum and moreover they represent about 30 times less the number of counts expected using the upper limit of Norman *et al.* [27]. In terms of inflection points, 10k counts correspond to 81.2 keV and 77.5 keV for the LogFT and BetaShape capture probabilities, respectively. Based on the error in the fit parameters, a 0.5 keV shift of the inflection point would have been observed. In reverse, a 0.5 keV left-shift is associated with about 425 EC counts which, given the vetoed acquisition settings, would have occurred along with 67.3 M  $\beta$  decays. An upper limit for the EC decays to the 82 keV level of  $^{176}\text{Yb}$  can be obtained from the ratio:

$$\frac{EC \text{ decays}}{\beta \text{ decays}} < \frac{425}{67.3 \times 10^6} = 6.3 \times 10^{-6}$$

Alternatively one can apply the counting statistics ap-

proach of Norman *et al.* [27] in the energy range from 60 keV to 110 keV where the vetoed spectrum consists of 22.3 k counts and the  $1\sigma$  upper limit is then  $\sqrt{2 \times 22.3k} = 212$  counts so that the above ratio EC decays over  $\beta$  decays is then  $< 3.2 \times 10^{-6}$ .

The energy range of interest to observe the K-shell captures to the ground state is from 40 keV to 80 keV, where 3.3 k counts are present in the vetoed spectrum. An analysis equivalent to the one above is however of little significance for the setting of an upper limit because of the substantially negligible K-shell capture probability. On the other hand, the upper limit found for the 5<sup>th</sup> forbidden EC to the 82 keV applies as well to the 7<sup>th</sup> EC to ground state, the latter being, in general terms, much less likely than the former.

### III. Q VALUE MEASUREMENT

#### A. Penning trap apparatus and measurement

The  $^{176}\text{Lu}$   $Q$ -value and mass excess measurements were performed at the Low Energy Beam and Ion Trap (LEBIT) facility at the National Superconducting Cyclotron Laboratory (NSCL) [58]. LEBIT is a Penning trap mass spectrometry (PTMS) facility that was designed for precise mass measurements with short-live radioactive isotopes produced via projectile fragmentation by the coupled cyclotron facility at the NSCL. However, it also includes two offline ion sources—a Laser Ablation Source (LAS) and a Thermal Ion Source (TIS)—that are used to produce ions of stable isotopes for calibration and reference purposes. These sources have also been used to produce long-lived isotopes for nuclear and neutrino physics studies. A schematic of the components of LEBIT relevant to the measurements described here is shown in Fig. 12.

In this work, the LAS was used to produce singly-charged  $^{176}\text{Lu}^+$ ,  $^{176}\text{Hf}^+$ , and also  $^{176}\text{Yb}^+$  ions from sheets of approximately  $25 \times 12 \times 1 \text{ mm}$  thick, naturally abundant lutetium, hafnium, and ytterbium samples. Sheets of two different materials were mounted side by side on the LAS target holder, which is connected to a stepper motor to enable selective production of ions of

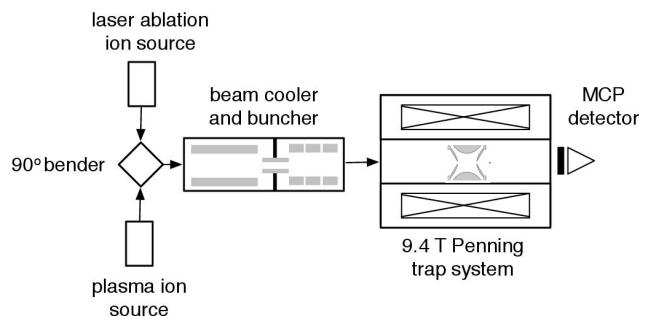


FIG. 12. A schematic of the sections of the LEBIT beamline used in this work.

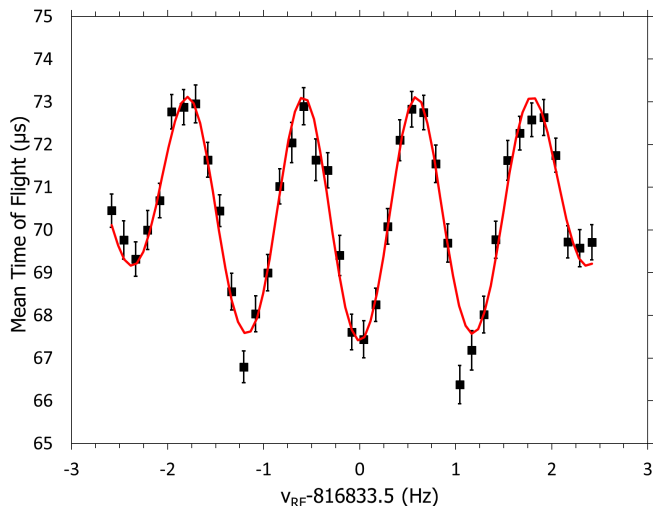


FIG. 13. A 1.0 s Ramsey ion cyclotron resonance for  $^{176}\text{Lu}$ . The solid line is the theoretical fit to the data.

two different isotopes during a single experimental run.

After production in the LAS, ions are transported to a beam cooler/buncher consisting of a helium gas filled RFQ ion guide and trap that is used to produce low emittance, short duration ion bunches. The ion bunches are then transported to the Penning trap where they are captured and the measurement is performed.

The LEBIT Penning trap has a hyperbolic trap structure, housed within a 9.4 T superconducting solenoidal magnet. LEBIT uses the Time of Flight-Ion Cyclotron Resonance (TOF-ICR) technique [59] to precisely measure the cyclotron frequency of ions within the trap:

$$f_c = \frac{qB}{2\pi m} \quad (2)$$

For this experiment, the Ramsey excitation scheme was used [60–62]. Ions within the trap are driven with two time-separated quadrupolar radiofrequency (rf) pulses with a frequency close to  $f_c$ . The ions are then released from the trap toward a microchannel plate detector (MCP), where their time-of-flight from the trap to the detector is measured. This measurement is repeated for a series of ion bunches, with the frequency of the rf pulse systematically varied around  $f_c$ . The resulting times-of-flight produce a resonance curve, an example of which is shown in Fig. 13 for  $^{176}\text{Lu}^+$ . The central minimum corresponds to  $f_c$  and can be obtained from a fit to the theoretical line shape.

To account for time-related frequency shifts, cyclotron frequency measurements, like the one presented in Fig. 13, are alternately taken for the two isotopes in the LAS. By measuring the frequency of ion one at time  $t_1$ , ion two at time  $t_2$ , and ion one again at time  $t_3$ , the two cyclotron frequency measurements for ion one,  $f_{c1}(t_1)$  and  $f_{c1}(t_3)$ , can be linearly interpolated to find  $f_{c1}(t_2)$  at time  $t_2$ . This is then used to find the cyclotron

TABLE IV. Measured cyclotron frequency ratios for combinations of  $^{176}\text{Lu}^+$ ,  $^{176}\text{Hf}^+$ , and  $^{176}\text{Yb}^+$  ions among themselves. N is the number of individual ratio measurements contributing to the average,  $\bar{R}$ . The uncertainties for  $\bar{R}$ , shown in parentheses, have been inflated by the Birge Ratio, BR, when  $\text{BR} > 1$ .

Ratio	Ion Pair	N	BR	$\bar{R}$
(i)	$^{176}\text{Lu}^+ / ^{176}\text{Hf}^+$	94	1.1	0.999 992 725 1(41)
(ii)	$^{176}\text{Lu}^+ / ^{176}\text{Yb}^+$	62	1.1	0.999 999 335 5(47)
(iii)	$^{176}\text{Hf}^+ / ^{176}\text{Yb}^+$	38	1.2	0.999 993 380 4(26)

frequency ratio of the two ions:

$$R = \frac{f_{c1}(t_2)}{f_{c2}(t_2)} = \frac{m_2}{m_1}. \quad (3)$$

The alternating measurements are repeated a number of times (in this work up to 94 times—see Table IV) and the average ratio,  $\bar{R}$ , and Birge Ratio [63] for the data set are calculated. When the Birge Ratio is greater than one, the uncertainty in  $\bar{R}$  is inflated by the Birge Ratio to account for possible underestimation of the statistical uncertainty. The average ratio,  $\bar{R}$  can then be used to directly calculate the  $Q$ -value of the decay, as discussed in Section III B.

## B. $^{176}\text{Lu}$ $\beta$ -decay $Q$ value

The three average cyclotron frequency ratios measured in this work are given in Table IV. The uncertainties given in the table have been inflated by the Birge Ratio of the measurement (also given) to conservatively account for a possible underestimate of the uncertainties.

The ratios in Table IV were used to directly obtain the  $Q$ -value of the decay between relevant parent and daughter nuclides i.e. the  $\beta$ -decay of  $^{176}\text{Lu}$  to  $^{176}\text{Hf}$ , the EC-decay of  $^{176}\text{Lu}$  to  $^{176}\text{Yb}$ , and the  $2\beta$ -decay of  $^{176}\text{Yb}$  to  $^{176}\text{Hf}$ , via

$$Q = (M_p - M_d)c^2 = (M_d - m_e)(1 - \bar{R})c^2, \quad (4)$$

where  $M_p$  is the mass of the parent atom,  $M_d$  is the mass of the daughter atom,  $m_e$  is the mass of the electron, and  $\bar{R}$  (previously defined in Eqn. (3) is such that ion 1 refers to the parent, and ion 2 the daughter. The ionization energies of the parent and daughter atoms are two orders of magnitude smaller than the statistical uncertainty, and are therefore ignored in this work.

The main goal of this work was to precisely determine the  $^{176}\text{Lu}$   $\beta$ -decay  $Q$ -value. From the data in Table IV, this  $Q$ -value can also be obtained by taking the ratio of ratios (ii) and (iii) to obtain an independent measurement of  $\bar{R}$  for  $^{176}\text{Lu}^+ / ^{176}\text{Hf}^+$  and again using Eqn. (4). All of the obtained  $Q$ -values, along with the values from the AME 2020 [64], are given in Table V. The measured  $Q$ -values are in good agreement with the AME 2020, but

are more precise, with all of the new measurements having an uncertainty  $< 1$  keV.

The  $^{176}\text{Lu}$   $\beta$ -decay  $Q$ -value can be used to determine the end point energies for the primary (99.61%), and secondary (0.39%) branches to the 596.82(5) keV  $6^+$  and 997.73(6) keV  $8^+$  levels, respectively in  $^{176}\text{Hf}$  [26]. The resulting end-point energies are given in Table VI.

### C. $^{176}\text{Lu}$ and $^{176}\text{Hf}$ atomic masses

From a PTMS measurement at Florida State University, the atomic mass of  $^{176}\text{Yb}$  is known to a precision of 14 eV. Thus, using ratios (ii) and (iii) in Table IV and the atomic mass of  $^{176}\text{Yb}$ , it was possible to determine the absolute masses of  $^{176}\text{Lu}$  and  $^{176}\text{Hf}$ , using the equation

$$M = (M_{\text{Yb}} - m_e)\bar{R}^{-1} + m_e, \quad (5)$$

where  $M$  is the mass of atom to be determined ( $^{176}\text{Lu}$  or  $^{176}\text{Hf}$ ),  $M_{\text{Yb}}$  is the mass of  $^{176}\text{Yb}$ , and  $\bar{R}$  is the appropriate ratio, (ii) or (iii) from Table IV, for  $^{176}\text{Lu}$  or  $^{176}\text{Hf}$ , respectively. The resulting masses are reported in Table VII as mass excesses, which are calculated from

$$\text{ME} = (M - A) \times 931.4940954(57) (\text{keV}/c^2)/u, \quad (6)$$

where  $A = 176$  is the mass number of the ion of interest and the conversion factor between  $\text{keV}/c^2$  and  $u$  is from Ref. [65]. The mass excesses we obtain in this work are in good agreement with the AME2020 values, which come primarily from  $(n, \gamma)$  and  $\beta^-$ -decay measurements that link  $^{176}\text{Lu}$  and  $^{176}\text{Hf}$  to  $^{174}\text{Yb}$ , which has been precisely measured with the Florida State University Penning trap. The results are in good agreement with other, less precise, measurements performed with the TRIGA-TRAP Penning trap [25]. Here we have reduced the uncertainties by factors of 1.5 and 3 for  $^{176}\text{Lu}$  and  $^{176}\text{Hf}$ , respectively, and in each case the uncertainties are both now  $< 1$  keV/ $c^2$ .

TABLE V.  $Q$ -values for  $^{176}\text{Lu}$   $\beta$ -decay or EC-decay and  $^{176}\text{Yb}$  2EC-decay calculated from cyclotron frequency ratios listed in Table IV. The calculated  $Q$ -value is listed along with the AME 2020 value [64] and the difference  $\Delta Q = Q_{\text{LEBIT}} - Q_{\text{AME}}$ .

Decay	Ratio	$Q$ -value (keV)		$\Delta Q$ (keV)
		LEBIT	AME2020	
$^{176}\text{Lu}(\beta^-)$	(i)	1192.28(67)		-1.8 (11)
	(ii)/(iii)	1193.78(88)	1194.09(87)	-0.3(12)
	Avg.	1193.03(55)		-1.1(10)
$^{176}\text{Lu}(\text{EC})$	(ii)	108.90(76)	109.0(12)	-0.1(14)
$^{176}\text{Yb}(2\beta^-)$	(iii)	1084.88(43)	1085.1(15)	-0.2(15)

TABLE VI.  $\beta$ -spectrum end-point energies from this work deduced with the data from [26] for the primary and secondary decays of  $^{176}\text{Lu}$  to  $6^+$  and  $8^+$  levels in  $^{176}\text{Hf}$ .

$J^\pi$	Daughter level		$\beta$ end point (keV)
	$E^*$ (keV)	Branch Strength	
$6^+$	596.82(5)	99.61 %	596.21(55)
$8^+$	997.73(6)	0.39 %	195.30(55)

TABLE VII. Mass excesses, ME, for  $^{176}\text{Lu}$  and  $^{176}\text{Hf}$ , obtained from the ratios listed in Table IV. The results are compared to those listed in the AME2020 [64]. The column  $\Delta M$  is calculated as  $\text{ME}_{\text{LEBIT}} - \text{ME}_{\text{AME}}$

Nuclide	ME (keV/ $c^2$ )		$\Delta M$ (keV/ $c^2$ )
	LEBIT	AME	
$^{176}\text{Lu}$	-53 382.42(76)	-53 382.3(12)	-0.1(14)
$^{176}\text{Hf}$	-54 576.20(43)	-54 576.4(15)	0.2(15)

## IV. $\beta$ -SPECTRUM CALCULATIONS

Theoretical calculations of the two first forbidden non-unique transitions of  $^{176}\text{Lu}$  have been performed within the framework of the formalism described by Behrens and Bühring in [66] based on Fermi theory. The general expression of the  $\beta$  spectrum in this low-energy effective theory of the weak interaction is given, in relativistic units ( $\hbar = m_e = c = 1$ ), by

$$\frac{dN}{dW} = \frac{G_\beta^2}{2\pi^3} F(Z, W) p W (W_0 - W)^2 C(W) X(W) \quad (7)$$

where  $G_\beta$  is the Fermi coupling constant;  $W$  is the total  $\beta$  particle energy and  $p$  its momentum;  $W_0$  is the maximum available total energy;  $pW(W_0 - W)^2$  is the statistical shape that comes from the sharing of the momentum between the emitted leptons; and  $F(Z, W)$  is the Fermi function that takes into account the Coulomb interaction between the  $\beta$  particle and the daughter nucleus.

The shape factor  $C(W)$  is a convolution of the nuclear structure and the lepton dynamics determined from a multipole expansion of the hadron and lepton currents, expressed as

$$C(W) = \sum_{K, k_e, k_\nu} \lambda_{k_e} \left[ M_K^2(k_e, k_\nu) + m_K^2(k_e, k_\nu) - \frac{2\mu_{k_e} \gamma_{k_e}}{k_e W} M_K(k_e, k_\nu) m_K(k_e, k_\nu) \right]. \quad (8)$$

Quantities labeled by the lepton quantum numbers  $k_e$  and  $k_\nu$  depend on the relativistic wave functions, with in particular  $\lambda_1 = 1$ . The main multipole order  $K$  comes from the expansion of the nuclear current. We followed [67] for the calculation of  $C(W)$ , considering the dominant terms with  $K = 1, 2$  and  $k_e + k_\nu = 2, 3$ . The lepton wave functions are expanded in powers of  $(m_e R)$ ,  $(WR)$  and  $(\alpha Z)$ , with  $R$  the nuclear radius and  $\alpha$  the fine

structure constant. This procedure avoids the calculation of overlaps between nuclear and lepton wave functions and the nuclear matrix elements, also called form factor coefficients, become independent of the lepton momenta. All the formulas used in the present work, assuming impulse approximation, are well described in [67].

The factor  $X(W)$  stands for some additional corrections. The first one is for the atomic screening effect. The Fermi function and the  $\lambda_{k_e}$  parameters directly depend on the electron wave functions, which have been determined as described in [12], i.e. considering the Coulomb potential generated by a uniformly charged sphere. The simplicity of such a potential makes possible the expansion of the lepton wave functions as described previously, but it prevents us including directly any screened potential. In a previous work [68], we developed a dedicated code for a full numerical calculation of the electron wave functions taking into account such screened potentials. In the present work, we have tabulated beforehand screened-to-unscreened ratios of  $F(Z, W)$  and  $\lambda_{k_e}$  at the required energies and corrected these quantities to account for screening in the  $\beta$  spectrum.

The second correction corresponds to the atomic exchange effect. Correction of this effect for  $k_e = 1$  has been determined as described in [68] for the atomic  $s_{1/2}$  orbitals and as complemented in [69] for the  $p_{1/2}$  orbitals. This effect has recently been extended to the forbidden unique transitions as briefly described in [70] and we have used this formulation to determine the correction for  $k_e = 2$ . Again, the correction factors have been tabulated beforehand at the required energies and applied during the  $\beta$  spectrum calculation. Finally, radiative corrections are also included in  $X(W)$ . They are calculated as described in [71] and as a benchmark, we obtained excellent agreement with those determined in the survey of superallowed  $\beta$  transitions in [72].

A realistic description of a nuclear state can be achieved via configuration mixing. Its many-particle wave function then results from a linear combination of single-particle (nucleon) wave functions. In  $\beta$  decay, the transition amplitude between the initial and final nuclear states is determined by evaluating the corresponding one-body spherical tensor operator  $T_\lambda$ . It can be expressed as a weighted sum of the single-particle transition amplitudes [73]:

$$\langle \xi_f J_f || T_\lambda || \xi_i J_i \rangle = \hat{\lambda}^{-1} \sum_{a,b} \langle a || T_\lambda || b \rangle \langle \xi_f J_f || [c_a^\dagger \tilde{c}_b]_\lambda || \xi_i J_i \rangle \quad (9)$$

where  $\hat{\lambda}$  is the tensor rank,  $\langle a || T_\lambda || b \rangle$  is a single-particle matrix element describing a nucleon-nucleon transition, and  $\langle \xi_f J_f || [c_a^\dagger \tilde{c}_b]_\lambda || \xi_i J_i \rangle$  is the one-body transition density.

The list of nucleon-nucleon transitions and their one-body transition densities have been determined employing the shell model code NuShellX@MSU [74]. Above a doubly-magic  $^{132}\text{Sn}$  core, we selected the  $jj56pn$  valence space and used the recommended  $khhe$  effective interaction [75]. Proton valence space spans from  $1g_{7/2}$  to  $1h_{11/2}$ , in which 21 particles have to be distributed for

$^{176}\text{Lu}$  and 22 for  $^{176}\text{Hf}$ . Neutron valence space spans  $1h_{9/2}$  to  $1i_{13/2}$ , in which 23 particles have to be distributed for  $^{176}\text{Lu}$  and 22 for  $^{176}\text{Hf}$ . Such a high number of particles leads to a non-tractable number of possible configurations. We have thus limited the valence space by assuming completely full the lowest orbitals, i.e.  $1g_{7/2}$ ,  $2d_{5/2}$  and  $2d_{3/2}$  for protons and  $1h_{9/2}$  and  $2f_{7/2}$  for neutrons. Other orbitals have been left free. The one-body transition densities have been calculated for the dominant  $K$  values and are given in Table VIII for the main transition.

We followed the method depicted in [76] to estimate the harmonic oscillator frequencies required for the calculation of the single-particle matrix elements. To this purpose, the experimental root mean square charge radii of  $^{176}\text{Lu}$  and  $^{176}\text{Hf}$  have been taken in [77] and the nucleon configurations provided by NuShellX have been employed. We obtained  $(\hbar\omega)_n = 7.594$  MeV for the initial neutrons and  $(\hbar\omega)_p = 6.833$  MeV for the final protons. The equivalent uniform charge radii have been deduced and used in the calculations:  $R_i(\text{Lu}) = 6.868$  fm and  $R_f(\text{Hf}) = 6.808$  fm.

The  $\beta$ -decay formalism is totally relativistic due to the small rest mass of the  $\beta$  particle, leading to particle wave functions with small and large components. In addition, the weak interaction is described by a linear combination of vector and axial-vector components. This results in different matrix elements that can be either vector or axial-vector, non-relativistic when only large components of the nucleon wave functions are needed, or relativistic when small components are involved. In the expansion of  $M_K(k_e, k_\nu)$  in [67], one can see that in the present case appears the relativistic vector nuclear matrix element  ${}^V F_{101}$ , for which an accurate value is of importance.

However, NuShellX is a non-relativistic nuclear structure model. One could identify the large component of the nucleon wave function to the non-relativistic wave function and estimate the small component from the large one, but the inaccuracy of such an approach has been seen for decades (see e.g. [78]). Another approach is to assume the conserved vector current hypothesis (CVC) that comes from gauge invariance of the weak interaction. One can then relate  ${}^V F_{101}$  to the non-relativistic form factor coefficient  ${}^V F_{110}$  by [66]

$${}^V F_{101} \simeq -\frac{R}{\sqrt{3}} (W_0 - (m_n - m_p) + \Delta E_C) {}^V F_{110} \quad (10)$$

with  $m_n$  and  $m_p$  the neutron and proton rest masses and  $\Delta E_C$  the Coulomb displacement energy. Considering a uniformly charged sphere, the latter quantity is expressed by the usual formula

$$\Delta E_C^{(1)} = \frac{6}{5} \frac{\alpha Z_f}{R_f} = 18.273 \text{ MeV}. \quad (11)$$

One can also go back to the derivation of this formula and establish another one that depends on the initial and final

TABLE VIII. One-body transition densities (OBTD) of the dominant multipole orders in the main  $\beta$  transition of  $^{176}\text{Lu}$  decay, as given by NushellX. Coulomb displacement energy for each nucleon-nucleon transition is also given.

neutron	$\rightarrow$	proton	OBTD	$\Delta E_C^{(3)}$ (MeV)
$K = 1$				
$3p_{3/2}$	$\rightarrow$	$3s_{1/2}$	0.01779	15.415
$3p_{1/2}$	$\rightarrow$	$3s_{1/2}$	0.05171	15.415
$1i_{13/2}$	$\rightarrow$	$1h_{11/2}$	-0.83750	15.957
$K = 2$				
$2f_{5/2}$	$\rightarrow$	$3s_{1/2}$	0.01600	15.006
$3p_{3/2}$	$\rightarrow$	$3s_{1/2}$	0.02385	14.631
$1i_{13/2}$	$\rightarrow$	$1h_{11/2}$	-0.00769	15.551

nuclear radii:

$$\Delta E_C^{(2)} = \frac{3}{5} \frac{\alpha}{R_f} Z_f(Z_f - 1) - \frac{3}{5} \frac{\alpha}{R_i} Z_i(Z_i - 1) = 23.460 \text{ MeV} \quad (12)$$

where we used  $R_i(\text{Lu})$  and  $R_f(\text{Hf})$  as given above. It is noteworthy that a constant  $\Delta E_C$  for every nucleon-nucleon transition is an approximation. The Coulomb displacement energy was demonstrated a long time ago to possibly be sensitive to the mismatch between the initial and final nucleon wave functions [79]. As described in [66], we have assumed that the single-particle potential difference is determined by the average of the Coulomb potential  $V(r)$  only:

$$\Delta E_C^{(3)} = \frac{\int_0^\infty g_f V(r) g_i (r/R)^K r^2 dr}{\int_0^\infty g_f g_i (r/R)^K r^2 dr} \quad (13)$$

where  $g_i$  and  $g_f$  are the radial large components of the initial and final nucleon wave functions, respectively. The calculated values for the different nucleon-nucleon transitions of interest in this work are given in Table VIII.

We present in Fig. 14 the spectra of the main transition calculated with the three different methods for determining  $\Delta E_C$ . We have considered the free-nucleon value of  $g_A$ , i.e.  $g_A^{\text{free}} = 1.2763(15)$  as the result of the mean of two recent precise measurements [80, 81]. These spectra are compared to the measurement from this work and to an allowed spectrum, for which  $C(W) = 1$ . Indeed, first forbidden non-unique transitions are usually treated as allowed when the  $\xi$ -approximation is fulfilled, i.e.  $\alpha Z/R \gg (W_0 - 1)$  [12]. If including nuclear structure is clearly important, we also see the great influence of the sole Coulomb displacement energy.

The value of the axial-vector coupling constant  $g_A$  has been shown to potentially influence the spectrum shape of forbidden non-unique transitions, sometimes significantly [13, 82, 83]. Indeed, an adjustment may be necessary to reproduce some experimental observables because

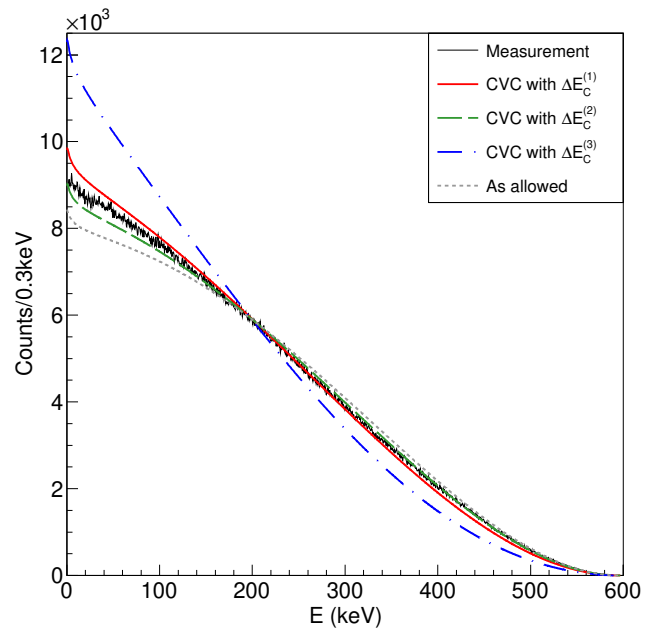


FIG. 14. The measured  $\beta$  spectrum of the main transition in  $^{176}\text{Lu}$  decay is compared to four different calculations. Theoretical spectra with nuclear structure have been computed using the CVC hypothesis and three different methods to determine the Coulomb displacement energy  $\Delta E_C$ . The free-nucleon value of  $g_A$  has been considered.

the nucleon-nucleon transition occurs in nuclear matter. A quenched value of  $g_A$  can then take up a part of the mismodeling of nuclear structure, e.g. an approximate treatment of the many-nucleon correlations. Following a recent review [84], one can deduce a quenching factor for  $^{176}\text{Lu}$  decay from the quenching factor in infinite nuclear matter and estimate an effective value of  $g_A^{\text{est}} = 1.1075$ .

As some of our spectra with  $g_A^{\text{free}}$  are not so far from the experimental spectrum, we have applied the “spectrum shape method” proposed in [85] to extract an effective  $g_A$  value. We tried four possibilities: first, we kept  $g_A^{\text{free}}$  and we adjusted the Coulomb displacement energy; next,  $g_A$  was adjusted for the different  $\Delta E_C$ . Each possibility was found to give very similar agreement with the measurement and close standardized residuals. We present in Fig. 15 one of the results and the adjusted values are given in Table IX. Uncertainties on the parameters come from the fit procedure and also include the influence of the energy range considered. As expected, the value of  $g_A$  strongly depends on the assumed Coulomb displacement energy used in CVC. The usual formula  $\Delta E_C^{(1)}$  gives the closest effective value to  $g_A^{\text{est}}$ . It is noteworthy that a non-linear trend clearly remains in the standardized residuals, even if the latter lie within  $\pm 2\sigma$ .

The  $\log f$  values corresponding to each adjustment are also given in Table IX, where the uncertainties also includes the component due to the maximum energy. One can see that they are systematically negative but widely spread. The mean value is  $\log f = -0.91(14)$ . From the

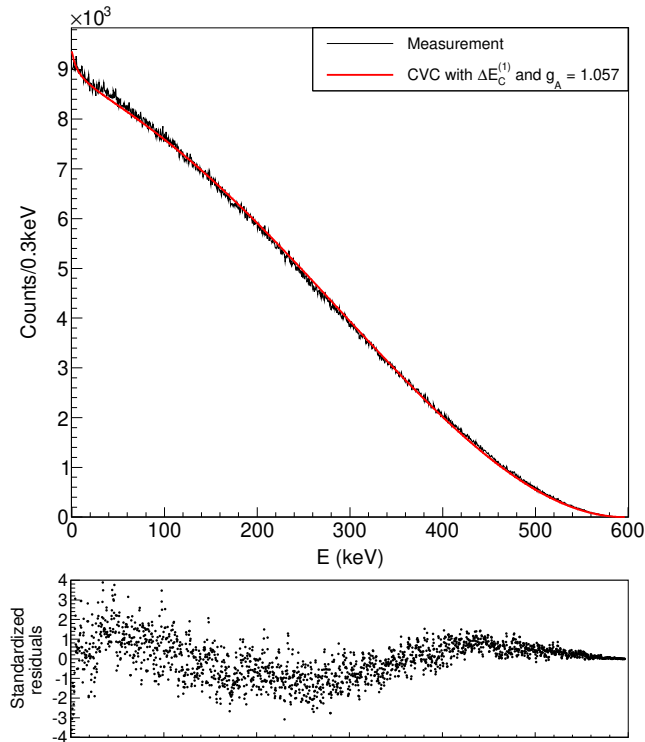


FIG. 15. Theoretical spectrum of the main transition in  $^{176}\text{Lu}$  decay. An effective  $g_A$  constant has been fitted to reproduce at best the measured spectrum. A non-linear trend clearly remains in the standardized residuals.

partial half-life, evaluated from experimental results for the branching ratio and the total decay half-life [26], one can deduce for this transition  $\log ft = 17.17(14)$ . This value is lower than in [26] where the transition was calculated as allowed with the LogFT code [56], leading to a  $\log f$  value of 1.093(2).

Finally, one has to mention that we have not been able to reproduce the measured spectrum of the second  $\beta$  transition to the  $8^+$  state of  $^{176}\text{Hf}$ . In addition, the spectrum shape has not been found to be sensitive to the  $g_A$  value. The valence space in NushellX is probably too much constrained to obtain a realistic description of this nuclear state. As the calculations depend on the nuclear structure, the sensitivity of this  $\beta$  transition to  $g_A$  is not conclusive.

## V. DISCUSSION AND CONCLUSIONS

Coupled with present knowledge of scintillation processes, the relatively large natural activity in Lu-containing scintillators, has enabled precise observation of  $\beta$  emissions of  $^{176}\text{Lu}$  and a much stricter formulation of the upper limit of its EC decay branches. Experimental shaping factors for the entire energy range of the

TABLE IX. Adjusted values that lead in each case to similar spectra and standardized residuals as shown in Fig. 15. The corresponding reduced- $\chi^2$  and  $\log f$  values are also given.

$\Delta E_C$ (MeV)	$g_A$	reduced- $\chi^2$	$\log f$
20.527(46)	$g_A^{\text{free}}$	1.278	-0.835(19)
$\Delta E_C^{(1)}$	1.057(4)	1.258	-0.975(14)
$\Delta E_C^{(2)}$	1.560(5)	1.296	-0.679(12)
$\Delta E_C^{(3)}$	0.834(3)	1.227	-1.148(14)

dominant  $\beta$  transition of  $^{176}\text{Lu}$ , with a statistics of 8.5 M counts, have been made available. Moreover, even the least probable beta transition of  $^{176}\text{Lu}$  was measured in its entire energy range and shape factors formulated, albeit with a counting statistic limited to 83 k counts. As a result of efforts dedicated to observe EC decays a new upper limits was established for their branching ratios, confining their probability by almost 3 orders of magnitude.

The presently implemented self-scintillation method for  $^{176}\text{Lu}$  provided unmatched results, made robust by independent experimental measurements and theoretical evaluations. Nevertheless room for further improvements exist. These include: the use of a coincidence spectrometer with enhanced energy resolution compared to NaI(Tl) for a more selective generation of gates; the use of a synchronized dual-channel signal-digitalization system allowing post-acquisition processing of coincidence; an improved pen-type PMT or an alternative scintillation light readout as SiPM, for enhancing energy resolution of the  $\beta$  spectroscopy and improve noise performances. Use of custom geometry of Lu-containing scintillator can also be considered. Small detector effects have been assessed empirically and the result allowed to neglect them in the response function. Although satisfactory in the present experiments, this result might benefit from further investigations both experimental and by means of simulations.

The Penning trap measurements performed in this work provide the first direct measurement of the  $^{176}\text{Lu}$   $\beta$ -decay Q value. Along with the energies of the  $6^+$  and  $8^+$  daughter levels in  $^{176}\text{Hf}$ , the results provide precise end-point energies for the  $\beta$ -spectra of the two  $^{176}\text{Lu}$  decay branches.

For the dominant  $\beta$  transition, the precision of the end point obtained by Penning trap measurements, i.e. 596.21(55) keV, validates the value obtained by self-scintillation of 596.6(9) keV. Similarly for the minor beta transition, the end point value of 195.30(55) keV obtained by Penning trap measurements validates that of 195.7(25) keV by self-scintillation.

Our theoretical study of the main transition in  $^{176}\text{Lu}$   $\beta$  decay have led to very different effective  $g_A$  values and the residuals in Fig. 15 indicate that part of the shape is not well reproduced. A possible improvement of our modeling would be a more accurate treatment of the lepton current, e.g. with next-to-leading-order terms as in [85], that could make the spectrum shape less sensitive to the



Coulomb displacement energy.

One might think about looking at partial half-lives,  $t_{1/2}$ , to select the adjustment that gives the best value. However, our study is based on a nuclear structure determined with a spherical shell model while  $^{176}\text{Lu}$  is well known to be strongly deformed. This leads to a hindered transition rate such as [86]

$$t_{1/2}^{\text{exp}} = t_{1/2}^{\text{theo}} / [F^{\Delta K - 1}]^2 \quad (14)$$

where  $K$  is the appropriate quantum number corresponding to the projection of the total angular momentum on the symmetry axis ( $\Delta K = 7$  in our case), and  $F \simeq 0.15$  is the reduction factor as determined in [86]. The four adjustments we have performed lead to  $t_{1/2}^{\text{theo}}$  values that can differ by up to a factor of three, but which are 13 orders of magnitude smaller than  $t_{1/2}^{\text{exp}}$ . From these results, we deduced a reduction factor of  $F = 0.0768(20)$ . The adjusted  $g_A$  value with  $\Delta E_C^{(1)}$  gives the best corrected partial half-life but  $g_A^{\text{free}}$  with  $\Delta E_C$  adjusted gives a very close value. A detailed analysis of  $^{176}\text{Lu}$  decay with a realistic nuclear structure that includes nucleus deformation is therefore required to extract a firm effective  $g_A$  constant.

## ACKNOWLEDGMENTS

This research was supported by Michigan State University and the Facility for Rare Isotope Beams and the National Science Foundation under Contracts No. PHY-1102511 and No. PHY-1307233. This material is based upon work supported by the US Department of Energy, Office of Science, Office of Nuclear Physics under Award No. DE-SC0015927. The work leading to this publication has also been supported by a DAAD P.R.I.M.E. fellowship with funding from the German Federal Ministry of Education and Research and the People Programme (Marie Curie Actions) of the European Union's Seventh Framework Programme (FP7/2007/2013) under REA Grant Agreement No. 605728.

Part of the experimental work of the  $\beta$  spectra measurement was performed as part of the EMPIR Project 15SIB10 MetroBeta. This project has received funding from the EMPIR program co-financed by the Participating States and from the European Union's Horizon 2020 research and innovation program.

The theoretical work was performed as part of the EMPIR Project 20FUN04 PrimA-LTD. This project has received funding from the EMPIR program co-financed by the Participating States and from the European Union's Horizon 2020 research and innovation program.

- 
- [1] J. Audouze, W. A. Fowler, and D. N. Schramm, *Nature Physical Science* **238**, 8 (1972).
- [2] M. Arnould, *Astronomy and Astrophysics* **22**, 311 (1973).
- [3] H. Beer, F. Kaeppler, K. Wisshak, and R. A. Ward, *Astrophysical Journal Supplement Series* **46**, 295 (1981).
- [4] A. Battaglia, W. Tan, R. Avetisyan, C. Casarella, A. Gyurijinyan, K. Manukyan, S. Marley, A. Nystrom, N. Paul, K. Siegl, K. Smith, M. Smith, S. Strauss, and A. Aprahamian, *European Physical Journal A* **52** (2016), 10.1140/epja/i2016-16126-x.
- [5] A. Boudin and M. Dehon, *Geochimica et Cosmochimica Acta* **33**, 142 (1969).
- [6] P. Patchett and M. Tatsumoto, *Nature* **288**, 571 (1980).
- [7] R. Bast, E. Scherer, P. Sprung, K. Mezger, M. Fischer-Gödde, S. Taetz, M. Böhnke, H. Schmid-Beurmann, C. Münker, T. Kleine, and G. Srinivasan, *Geochimica et Cosmochimica Acta* **212**, 303 (2017).
- [8] I. Spalding and K. Smith, *Proceedings of the Physical Society* **79**, 787 (1962).
- [9] T. Brenner, S. Büttgenbach, W. Rupperecht, and F. Träber, *Nuclear Physics, Section A* **440**, 407 (1985).
- [10] R. Kaewuam, A. Roy, T. Tan, K. Arnold, and M. Barrett, *Journal of Modern Optics* **65**, 592 (2018).
- [11] A. D'yachkov, A. Gorkunov, A. Labozin, S. Mironov, V. Panchenko, V. Firsov, and G. Tsvetkov, *Optics and Spectroscopy* **128**, 289 (2020).
- [12] X. Mougeot, *Phys. Rev. C* **91**, 055504 (2015).
- [13] M. Haaranen, P. C. Srivastava, and J. Suhonen, *Phys. Rev. C* **93**, 034308 (2016).
- [14] A. C. Hayes, J. L. Friar, G. T. Garvey, G. Jungman, and G. Jonkmans, *Phys. Rev. Lett.* **112**, 202501 (2014).
- [15] A. C. Hayes and P. Vogel, *Annual Review of Nuclear and Particle Science* **66**, 219 (2016).
- [16] L. Hayen, J. Kostensalo, N. Severijns, and J. Suhonen, *Phys. Rev. C* **100**, 054323 (2019).
- [17] K. Kossert and X. Mougeot, *Applied Radiation and Isotopes* **101**, 40 (2015).
- [18] K. Kossert, J. Marganec-Galazka, X. Mougeot, and O. Nähle, *Applied Radiation and Isotopes* **134**, 212 (2018).
- [19] K. Kossert and X. Mougeot, *Applied Radiation and Isotopes* **168** (2021), 10.1016/j.apradiso.2020.109478.
- [20] M. Heyden and W. Wefelmeier, *Die Naturwissenschaften* **26**, 612 (1938).
- [21] W. F. Libby, *Phys. Rev.* **56**, 21 (1939).
- [22] D. Dixon, A. McNair, and S. Curran, *The London, Edinburgh, and Dublin Philosophical Magazine and Journal of Science* **45**, 683 (1954).
- [23] V. Prodi, K. F. Flynn, and L. E. Glendenin, *Phys. Rev.* **188**, 1930 (1969).
- [24] M. Wang, W. Huang, F. Kondev, G. Audi, and S. Naimi, *Chinese Physics C* **45** (2021), 10.1088/1674-1137/abddaf.
- [25] J. Ketelaer, G. Audi, T. Beyer, K. Blaum, M. Block, R. B. Cakirli, R. F. Casten, C. Droese, M. Dworschak, K. Eberhardt, M. Eibach, F. Herfurth, E. Minaya Ramirez, S. Nagy, D. Neidherr, W. Nörtershäuser, C. Smorra, and M. Wang, *Phys. Rev. C* **84**, 014311 (2011).
- [26] M. Basunia, *Nuclear Data Sheets* **107**, 791 (2006).
- [27] E. Norman, E. Browne, I. Goldman, and P. Renne, *Applied Radiation and Isotopes* **60**, 767 (2004).
- [28] O. Ott, K. Kossert, and O. Sima, *Applied Radiation and Isotopes* **70**, 1886 (2012), proceedings of the 18th International Conference on Radionuclide Metrology and

its Applications.

- [29] Y. Amelin and W. Davis, *Geochimica et Cosmochimica Acta* **69**, 465 (2005).
- [30] K. Zuber, *Physics Letters B* **485**, 23 (2000).
- [31] G. Beard and W. Kelly, *Nuclear Physics* **28**, 570 (1961).
- [32] F. Quarati, I. Khodyuk, C. van Eijk, P. Quarati, and P. Dorenbos, *Nucl. Instrum. Methods Phys. Res. A* **683**, 46 (2012).
- [33] F. Quarati, P. Dorenbos, and X. Mougeot, *Appl. Radiat. Isot.* **108**, 30 (2016).
- [34] R. Sandler, G. Bollen, K. Gulyuz, A. Hamaker, C. Izzo, D. Puentes, M. Redshaw, R. Ringle, S. Schwarz, and I. Yandow, in preparation (2019).
- [35] C. L. Melcher and J. S. Schweitzer, *IEEE Transactions on Nuclear Science* **39**, 502 (1992).
- [36] B. Minkov, *Functional Materials* **1**, 103 (1994).
- [37] D. Cooke, K. McClellan, B. Bennett, J. Roper, M. Whittaker, R. Muenchausen, and R. Sze, *Journal of Applied Physics* **88**, 7360 (2000), cited By 186.
- [38] M. Nikl, H. Ogino, A. Krasnikov, A. Beitlerova, A. Yoshikawa, and T. Fukuda, *physica status solidi (a)* **202**, R4 (2005).
- [39] W. Drozdowski, K. Brylew, A. J. Wojtowicz, J. Kisielewski, M. Świrkowicz, T. Łukasiewicz, J. T. de Haas, and P. Dorenbos, *Opt. Mater. Express* **4**, 1207 (2014).
- [40] P. Dorenbos, J. T. M. de Haas, and C. W. E. van Eijk, *IEEE Transactions on Nuclear Science* **42**, 2190 (1995).
- [41] S. A. Payne, W. W. Moses, S. Sheets, L. Ahle, N. J. Cherepy, B. Sturm, S. Dazeley, G. Bizarri, and W. Choong, *IEEE Transactions on Nuclear Science* **58**, 3392 (2011).
- [42] I. V. Khodyuk and P. Dorenbos, *IEEE Transactions on Nuclear Science* **59**, 3320 (2012).
- [43] I. V. Khodyuk, *Nonproportionality of inorganic scintillators*, Ph.D. thesis, Faculty of Applied Sciences, Delft University of Technology, The Netherlands (2013).
- [44] H. Alva-Sánchez, A. Zepeda-Barrios, V. Díaz-Martínez, T. Murrieta-Rodríguez, A. Martínez-Dávalos, and M. Rodríguez-Villafuerte, *Scientific Reports* **8** (2018), 10.1038/s41598-018-35684-x.
- [45] M. Berger, J. Hubbell, S. Seltzer, J. Chang, J. Coursey, R. Sukumar, D. Zucker, and K. Olsen, “Xcom: Photon cross section database (version 1.5),” (2010).
- [46] Kinheng Crystal Material Co. Ltd., Shanghai, China. [www.kinheng-crystal.com](http://www.kinheng-crystal.com).
- [47] Scionix Holland BV, Bunnik, The Netherlands. [www.scionix.nl](http://www.scionix.nl).
- [48] E. der Mateosian and A. Smith, *Phys. Rev.* **88**, 1186 (1952).
- [49] M. Berger, J. Coursey, M. Zucker, and J. Chang, “Estar, pstar, and astar: Computer programs for calculating stopping-power and range tables for electrons, protons, and helium ions,” (2005).
- [50] M. P. Prange, Y. Xie, L. W. Campbell, F. Gao, and S. Kerisit, *Journal of Applied Physics* **122**, 234504 (2017).
- [51] F. Quarati, M. Alekhin, K. Krämer, and P. Dorenbos, *Nuclear Instruments and Methods in Physics Research Section A: Accelerators, Spectrometers, Detectors and Associated Equipment* **735**, 655 (2014).
- [52] D. Wortman and J. Cramer, *Nuclear Instruments and Methods* **26**, 257 (1964).
- [53] P. Magain, in *ESO/ST-ECF Data Analysis Workshop* (1989) p. 205.
- [54] X. Mougeot, *Phys. Rev. C* **92**, 059902 (2015).
- [55] X. Mougeot, *Applied Radiation and Isotopes* **154**, 108884 (2019).
- [56] N. Gove and M. Martin, *Atomic Data and Nuclear Data Tables* **10**, 205 (1971).
- [57] X. Mougeot, *Appl. Radiat. and Isot.* **134**, 225 (2018).
- [58] R. Ringle, S. Schwarz, and G. Bollen, *Int. J. of Mass Spec.* **349**, 87 (2013).
- [59] G. Gräff, H. Kalinowsky, and J. Traut, *Zeit. Phys. A* **297**, 35 (1980).
- [60] G. Bollen, H.-J. Kluge, T. Otto, G. Savard, and H. Stolzenberg, *Nucl. Instrum. Meth. B* **70**, 490 (1992).
- [61] S. George, K. Blaum, F. Herfurth, A. Herlert, M. Kretzschmar, S. Nagy, S. Schwarz, L. Schweikhard, and C. Yazidjian, *Int. J. of Mass Spec.* **264**, 110 (2007).
- [62] M. Kretzschmar, *Int. J. of Mass Spec.* **264**, 122 (2007).
- [63] R. T. Birge, *Phys. Rev.* **40**, 207 (1932).
- [64] M. Wang, W. Huang, F. Kondev, G. Audi, and S. Naimi, *Chinese Physics C* **45**, 030003 (2021).
- [65] P. J. Mohr, D. B. Newell, and B. N. Taylor, *Rev. Mod. Phys.* **88**, 035009 (2016).
- [66] H. Behrens and W. Bühring, *Electron Radial Wave Functions and Nuclear Beta Decay* (Clarendon, Oxford, 1982).
- [67] H. Behrens and W. Bühring, *Nuclear Physics A* **162**, 111 (1971).
- [68] X. Mougeot and C. Bisch, *Phys. Rev. A* **90**, 012501 (2014).
- [69] E. Aprile, J. Aalbers, F. Agostini, M. Alfonsi, L. Althueser, F. D. Amaro, V. C. Antochi, E. Angelino, J. R. Angevaere, F. Arneodo, D. Barge, L. Baudis, B. Bauermeister, L. Bellagamba, M. L. Benabderrahmane, T. Berger, A. Brown, E. Brown, S. Bruenner, G. Bruno, R. Budnik, C. Capelli, J. M. R. Cardoso, D. Cichon, B. Cimmino, M. Clark, D. Coderre, A. P. Colijn, J. Conrad, J. P. Cussonneau, M. P. Decowski, A. Depoian, P. Di Gangi, A. Di Giovanni, R. Di Stefano, S. Diglio, A. Elykov, G. Eurin, A. D. Ferella, W. Fulgione, P. Gaemers, R. Gaior, M. Galloway, F. Gao, L. Grandi, C. Hasterok, C. Hils, K. Hiraide, L. Hoetzs, J. Howlett, M. Iacovacci, Y. Itow, F. Joerg, N. Kato, S. Kazama, M. Kobayashi, G. Koltman, A. Kopec, H. Landsman, R. F. Lang, L. Levinson, Q. Lin, S. Lindemann, M. Lindner, F. Lombardi, J. Long, J. A. M. Lopes, E. López Fune, C. Macolino, J. Mahlstedt, A. Mancuso, L. Manenti, A. Manfredini, F. Marignetti, T. Marrodán Undagoitia, K. Martens, J. Masbou, D. Masson, S. Mastroianni, M. Messina, K. Miuchi, K. Mizukoshi, A. Molinaro, K. Morā, S. Moriyama, Y. Mosbacher, M. Murra, J. Naganoma, K. Ni, U. Oberlack, K. Odgers, J. Palacio, B. Pelssers, R. Peres, J. Pienaar, V. Pizzella, G. Plante, J. Qin, H. Qiu, D. Ramírez García, S. Reichard, A. Rocchetti, N. Rupp, J. M. F. dos Santos, G. Sartorelli, N. Šarčević, M. Scheibelhut, J. Schreiner, D. Schulte, M. Schumann, L. Scotto Lavina, M. Selvi, F. Semeria, P. Shagin, E. Shockley, M. Silva, H. Simgen, A. Takeda, C. Therreau, D. Thers, F. Toschi, G. Trinchero, C. Tunnell, M. Vargas, G. Volta, H. Wang, Y. Wei, C. Weinheimer, M. Weiss, D. Wenz, C. Wittweg, Z. Xu, M. Yamashita, J. Ye, G. Zavattini, Y. Zhang, T. Zhu, J. P. Zopounidis, and X. Mougeot (XENON Collaboration), *Phys. Rev. D* **102**, 072004 (2020).
- [70] S. J. Haselschwardt, J. Kostensalo, X. Mougeot, and J. Suhonen, *Phys. Rev. C* **102**, 065501 (2020).
- [71] L. Hayen, N. Severijns, K. Bodek, D. Rozpedzik, and X. Mougeot, *Rev. Mod. Phys.* **90**, 015008 (2018).

- [72] I. S. Towner and J. C. Hardy, *Phys. Rev. C* **77**, 025501 (2008).
- [73] J. Suhonen, *From Nucleons to Nucleus: Concepts of Microscopic Nuclear Theory* (Springer, Berlin, 2017).
- [74] B. Brown and W. Rae, *Nuclear Data Sheets* **120**, 115 (2014).
- [75] E. K. Warburton and B. A. Brown, *Phys. Rev. C* **43**, 602 (1991).
- [76] I. Towner, J. Hardy, and M. Harvey, *Nuclear Physics A* **284**, 269 (1977).
- [77] I. Angeli and K. Marinova, *Atomic Data and Nuclear Data Tables* **99**, 69 (2013).
- [78] R. Sadler and H. Behrens, *Z. Phys. A* **346**, 25 (1993).
- [79] J. Damgaard and A. Winter, *Physics Letters* **23**, 345 (1966).
- [80] J. Liu, M. P. Mendenhall, A. T. Holley, H. O. Back, T. J. Bowles, L. J. Broussard, R. Carr, S. Clayton, S. Currie, B. W. Filippone, A. García, P. Geltenbort, K. P. Hickerson, J. Hoagland, G. E. Hogan, B. Hona, T. M. Ito, C.-Y. Liu, M. Makela, R. R. Mammei, J. W. Martin, D. Melconian, C. L. Morris, R. W. Pattie, A. Pérez Galván, M. L. Pitt, B. Plaster, J. C. Ramsey, R. Rios, R. Russell, A. Saunders, S. J. Seestrom, W. E. Sondheim, E. Tatar, R. B. Vogelaar, B. VornDICK, C. Wrede, H. Yan, and A. R. Young (UCNA Collaboration), *Phys. Rev. Lett.* **105**, 181803 (2010).
- [81] D. Mund, B. Märkisch, M. Deissenroth, J. Krempel, M. Schumann, H. Abele, A. Petoukhov, and T. Soldner, *Phys. Rev. Lett.* **110**, 172502 (2013).
- [82] J. Kostensalo and J. Suhonen, *Phys. Rev. C* **96**, 024317 (2017).
- [83] J. Kostensalo, M. Haaranen, and J. Suhonen, *Phys. Rev. C* **95**, 044313 (2017).
- [84] J. T. Suhonen, *Frontiers in Physics* **5**, 55 (2017).
- [85] M. Haaranen, J. Kotila, and J. Suhonen, *Phys. Rev. C* **95**, 024327 (2017).
- [86] H. Ejiri and T. Shima, *J. Phys. G: Nucl. Part. Phys.* **44**, 065101 (2017).